nature protocols

https://doi.org/10.1038/s41596-025-01284-z

Protocol

Integrated fluorescence light microscopy-guided cryo-focused ion beam-milling for in situ montage cryo-ET

Jie E. Yang [1,2,3], **Veronika Vrbovská** [4], **Joshua M. Mitchell**[5,6,11], **Tilman Franke**[7], **Bryan S. Sibert**[1,2,3], **Matt R. Larson** [1,2,3], **Alexander S. Hall** [8], **Alex Rigort** [7], **Deane F. Mosher**[5,6,9], **John Mitchels**[4] & **Elizabeth R. Wright** [1,2,3,9,10] ✉

Abstract

Cryogenic-electron tomography (cryo-ET) permits the in situ visualization of biological macromolecules at the molecular level. Owing to the variable thickness of cells, tissues and organisms, frozen specimens may need to be thinned by cryo-focused ion beam (FIB) milling to produce thin (<500 nm) cryo-lamellae suitable for cryo-ET. Locating regions of interest remains a challenge because untargeted milling can lead to inadvertent ablation and removal of regions of interest. Correlative light and electron microscopy, combined with cryo-FIB milling, can guide the identification of labeled targets in the cellular milieu. Multiple transfers between cryo-imaging instruments, cumbersome correlation algorithms, limited accuracy and low throughput have hindered the routine adoption of cryo-FIB milling within a multimodal correlative workflow for in situ structural biology. Here we present a workflow for 3D correlative cryo-fluorescence light microscopy-FIB-ET that streamlines fluorescence light microscopy-guided FIB milling, improving throughput while preserving both structural and contextual information. The complete integration of hardware and software described here minimizes sample contamination from cross-platform exchanges and greatly enhances the efficiency of 3D targeting in cryo-milling. We then describe procedures for implementing montage parallel array cryo-ET (MPACT), which can be easily adapted to any modern life-science transmission electron microscope. MPACT supports high-throughput cryo-ET acquisitions (10 tilt series in 1.5 h) for structure determination and comprehensive contextual understanding of macromolecules within their native surroundings. A complete session from sample preparation to MPACT data processing takes 5–7 d for an individual experienced in both cryo-EM and cryo-FIB milling.

Key points

- Coupling 3D correlative focused ion beam milling with montage cryo-electron tomography enables the precise localization of regions of interest deep within cells and the acquisition of larger fields of view that preserve high-resolution structural details.

- Single-pair region of interest-marker registration, combined with integrated software and hardware, enhances correlative milling workflows. Montage parallel array cryo-electron tomography produces montages and individual tile tomograms, thereby eliminating possible mechanical adjustments to the transmission electron microscope.

Key references

Hampton, C. M. et al. *Nat. Protoc.* **12**, 150–167 (2017): https://doi.org/10.1038/nprot.2016.168

Yang, J. E. et al. *J. Struct. Biol.* **213**, 107709 (2021): https://doi.org/10.1016/j.jsb.2021.107709

Sibert, B. S. et al. *J. Vis. Exp.* **175**, 10.3791/62992 (2021): https://doi.org/10.3791/62992

Yang, J. E. et al. *Nat. Methods* **20**, 1537 (2023): https://doi.org/10.1038/s41592-023-01999-5

Kim, J. Y. et al. *Microsc. Microanal.* **29**, 2127 (2023): https://doi.org/10.1093/micmic/ozad125

---

[1]Department of Biochemistry, University of Wisconsin, Madison, WI, USA. [2]Cryo-Electron Microscopy Research Center, Department of Biochemistry, University of Wisconsin, Madison, WI, USA. [3]Midwest Center for Cryo-Electron Tomography, Department of Biochemistry, University of Wisconsin, Madison, WI, USA. [4]Thermo Fisher Scientific Brno, Brno, Czech Republic. [5]Department of Biomolecular Chemistry, University of Wisconsin, Madison, WI, USA. [6]Department of Medicine, University of Wisconsin, Madison, WI, USA. [7]Thermo Fisher Scientific Planegg, Bavaria, Germany. [8]Thermo Fisher Scientific, Houston, TX, USA. [9]Morgridge Institute for Research, Madison, WI, USA. [10]DOE Great Lakes Bioenergy Research Center, University of Wisconsin, Madison, WI, USA. [11]Present address: Investigative Medicine, Homer Stryker M.D. School of Medicine, Western Michigan University, Kalamazoo, MI, USA. ✉e-mail: erwright2@wisc.edu

Introduction

Biological systems are complex, and understanding the intricate interactions that support life requires multiplexed analytical approaches. One structural biology technique that has gained prominence in cell biology research is cryo-electron tomography (cryo-ET). Cryo-ET is used for the molecular-level visualization of biological machinery in situ, providing insights into the complex interactions that occur in every cell[1,2]. Owing to electron beam penetration limitations in transmission electron microscopy (TEM), samples thicker than ~500 nm need to be thinned by either cryo-ultramicrotomy[3] or, more recently, cryo-focused ion beam (cryo-FIB) milling[4,5] to prepare thin (<500 nm) cryo-lamellae suitable for cryo-ET. While cryo-ET is powerful for visualizing the cogs of the biological machine, it remains challenging to determine the location of specific entities, especially when their structures are unknown. In comparison, fluorescent, multicolor labeling can provide spatial and temporal information about targeted macromolecules, supporting colocalization imaging experiments where two or more fluorophores can be visualized to reveal their respective positions in three dimensions (3D). Therefore, correlative light and electron microscopy (CLEM) technologies, combined with fluorescence light microscopy (FLM)-guided cryo-FIB micromachining, enable the efficient targeting of unknown structures within complex cellular environments, allowing them to be revisited in the TEM at high resolution[6,7].

Although dual-beam FIB-scanning electron microscopes generate high-fidelity two-dimensional (2D) surface representations, they do not natively provide 3D volume information without the use of serial sectioning. Recent advances in combining spatial information from FLM with cryo-FIB milling have facilitated site-directed cryo-FIB fabrication[5,8–10] of cellular lamellae suitable for 3D analysis by cryo-ET. Several factors can impact the success of cryo-FLM-FIB milling. Historically, cryo-FLM has been performed using external imaging systems[6,7,11–13]. This strategy requires transferring the same sample across multiple microscopes, which carries the risk of ice contamination, devitrification and physical damage. Owing to the increased number of grid handling steps in the external workflow, a good concentration and distribution of fiducial markers is essential for counteracting potential nonlinear deformations[7,9]. For these experiments, complicated 3D correlation algorithms are used. While elegant, the inherent complexity requires an adequate number of fiducials (at least five) near the region of interest (ROI) for accurate correlation to be applied[9,14]. This may reduce the practicality of this solution because it is considered cumbersome and time consuming. Second, frozen lamellae may warp from interactions with the ion beam[15,16] and cryo-crinkling of the supporting materials[17]. This type of deformation alters fiducial coordinate positions, rendering them unusable for registration and transformation. In recent years, FLM modules have been integrated into cryo-FIB–scanning electron microscopy (SEM)[8,18–20] to facilitate real-time FLM-guided FIB milling. This approach simplifies operations and minimizes grid contamination by limiting the number of sample exchanges between individual microscope systems. Despite substantial advances, the development of efficient high-throughput workflows to generate FLM-targeted lamellae has lagged behind gains in cryo-FIB automation[21–23]. Once machined, the 180–300 nm in z-thickness FIB-milled lamellae (with dimensions in xy ranging from 5 to 20 µm, depending on the cell size) of cellular landscapes provide significant opportunities for achieving greater contextual and high-resolution structural information of macromolecules in their native, in situ environment by cryo-ET[24,25]. To automate and increase the number of seamless FIB-milled lamellae mapped by cryo-ET, montage parallel array cryo-ET (MPACT or montage cryo-ET)[26] acquisition schemes are used.

Development of the Protocol

We have developed effective cryo-FLM-ET and cryo-FLM-FIB-ET protocols[6,7,26] and approaches[26] for near-native state structural studies of virus-infected or transfected mammalian cells. To further develop 3D correlated cryo-FIB milling workflows for studies of adherent and virus-infected cells, we introduced nontoxic, fluorescent, electron-dense microspheres (40 nm in diameter)[27] to the cells, allowing them to be identifiable by both cryo-FLM and cryo-SEM imaging[26]. This is similar to the application of in situ fiducial markers for 3D FIB milling[28].

To further extend the contextual information gained through correlative imaging, we developed a montage parallel array cryo-ET (MPACT) approach. MPACT can be used to collect and seamlessly stitch together adjacent tilt series, for example, covering ~7 × 6 µm^2 (4.6 Å pixel size) of neurons and other cells, virus-infected cells or large cellular lamellae. The montage tomograms may be either segmented for 3D rendering to provide an expanded cellular perspective or split into individual tile tilt series tiles used for subtomogram averaging (STA). In our case, respiratory syncytial virus fusion glycoproteins and matrix protein lattices were averaged to resolutions of sub-20 Å (ref. 26). The use of MPACT improved cryo-ET throughput (each 3 × 3 MPACT takes ~1.5 h to acquire in the TEM) and internalized microspheres supported on-the-fly milling adjustments; however, 3D correlative milling still relied on an external cryo-FLM and fiducial-based correlation with the FIB-SEM to place initial milling boxes.

Here, we present a detailed protocol (Fig. 1) to streamline 3D correlative cryo-FLM-FIB-MPACT using integrated hardware (internal FLM in the FIB-SEM) and software that smoothly

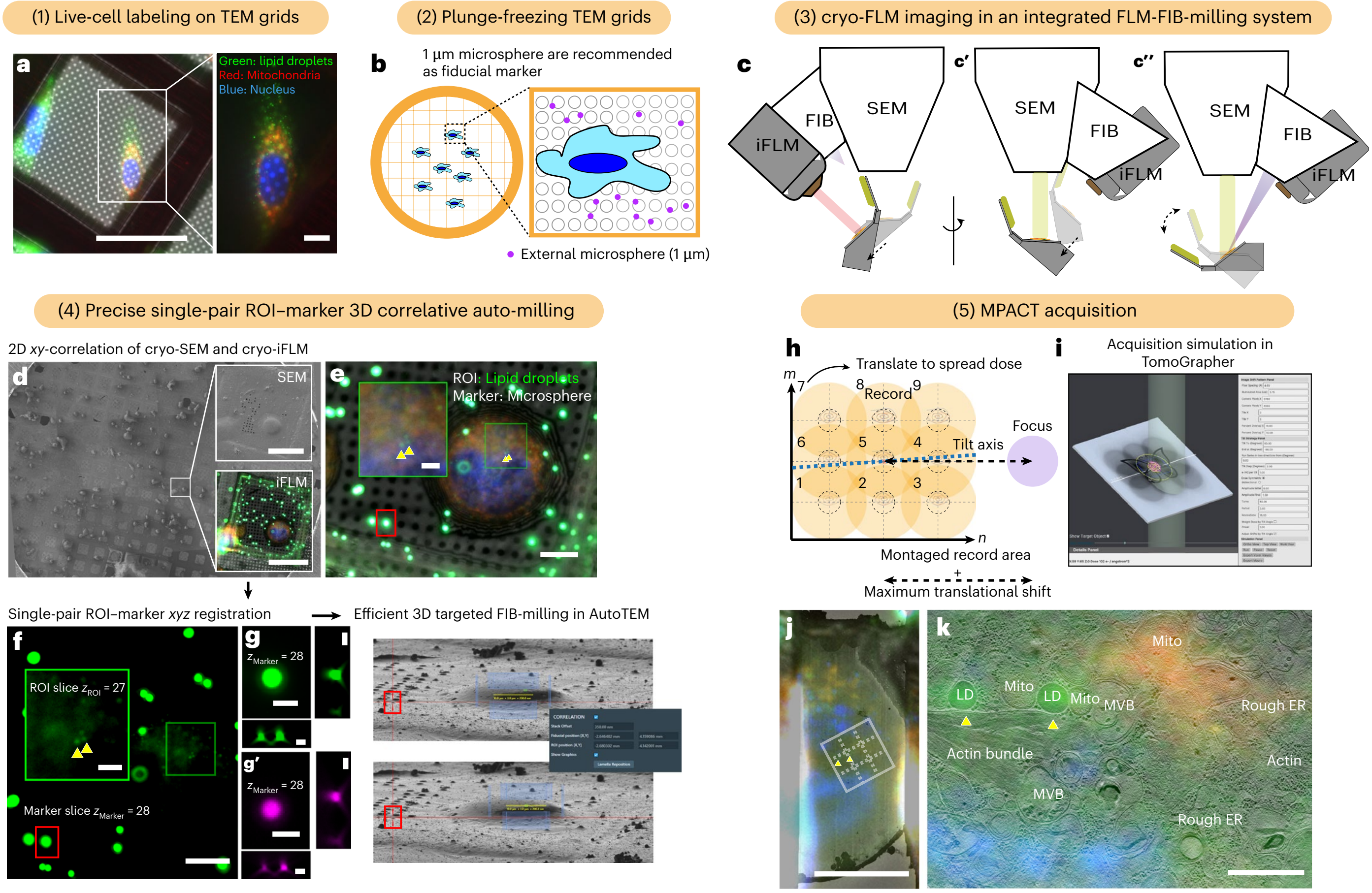

Fig. 1 | Overview for iFLM-guided cryo-FIB-milling for in situ montage cryo-ET. In a pictorial view, the main steps for correlative cryo-ET of cells using an integrated FLM-FIB milling system and MPACT are presented. **a**, Live-cell imaging of ROIs of a fluorescently labeled cell specimen cultured on the TEM grid before freezing (1). **b**, Fiducial markers added (1 µm FluoSpheres) to TEM grid before plunge-freezing (2). **c**, Cryo-FLM imaging of the labeled frozen grid using an integrated FLM-FIB-milling system (3). This involves the shuttle moving between FLM imaging (left) and FIB/SEM position (middle and right) positions via in-chamber translations and rotations. **d**–**g**, Identification of single-pair ROI–marker to perform 3D transformations for streamlined automated correlative FIB milling using MAPS and AutoTEM (4) The SEM (**d**) and FLM 3D stacks (**e**) are first acquired and correlated in the 2D *xy* plane prior to FIB milling. Assigning (**f**) and pairing (**g**) of the ROI and its associated marker in corresponding fluorescent and or reflection channels (**g′**) are performed to transform the ROI in the 3D *z* plane in MAPS. The milling boxes are then placed in AutoTEM based on the 3D transformation. **h**–**k,** Correlative montage cryo-ET acquisition via MPACT in SerialEM and subsequent data processing of ROIs (5): this step includes solutions that perform MPACT pattern design (**h**) and optimization in TomoGrapher (**i**), on-the-fly correlation and ROI identification (**j**) and processing from automated tilt series stitching and subsequent tomogram reconstruction (**k**), to data rendering (segmentation) and STA. MVB, multivesicular bodies; ER, endoplasmic reticulum; Mito, mitochondria; LD, lipid droplets. The yellow triangles point out a pair of LD as the targeted ROI, shown in **e**–**f**, **j** and **k.** Scale bars, 50 µm in **a** and **d**, 10 µm in **e** and **j**, 5 µm in **f**, 2 µm in **g** and 1 µm in **k**.

handles cross-module conversions. We illustrate the requirements needed for real-time, precise relocation of ROI using both conventional and FIB-etched fiducials. Specifically, for nonadherent mammalian cells such as eosinophils (EOS), the samples[29] are prepared by direct deposition. In contrast, adherent mammalian cells, including primary *Drosophila melanogaster* neurons[26,30,31], human alveolar basal epithelial A549 (ref. 26), human bronchial epithelium BEAS-2B[32] and HeLa cells[26], are cultured directly onto gold grids with an optional addition of 1 µm fluorescent microspheres before vitrification (Fig. 2; Steps 1–11). We collect cryo-FLM data using an integrated fluorescence light microscope (iFLM)-cryo-dual beam FIB-SEM (Aquilos 2) (Fig. 2; Steps 13–44) and perform 'single-pair ROI–marker' registration where the ROI *z* height is retrieved via its relative position to an unambiguously identified marker to setup the lamellae site for automated FIB milling. The entire correlation and milling process is fully integrated into MAPS Software and AutoTEM Software (Steps 25–44; Thermo Fisher Scientific). Once

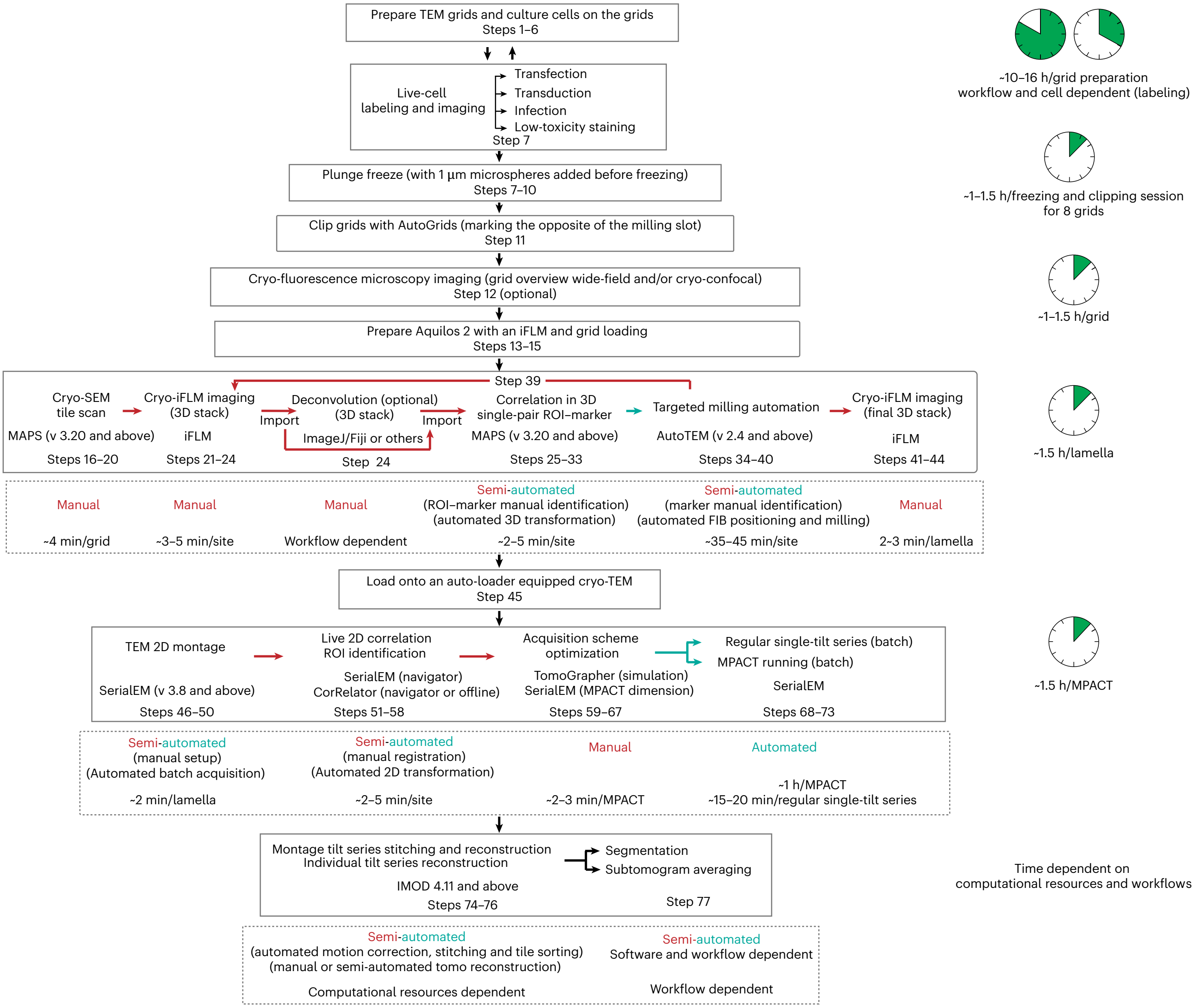

Fig. 2 | Flowchart of the steps for 3D-cryo-iFLM-FIB-MPACT protocol. The protocol describes the key steps involved in the precise 3D correlative FLM-guided FIB milling, coupled with montage cryo-ET acquisition via MPACT. The critical steps involved in iFLM-guided 3D correlative milling and MPACT acquisition are described using color-coded arrows and automation levels (red, manual or semi-manual; green, automated). The time frames for the whole workflow and individual steps in iFLM-guided 3D correlative milling and MPACT acquisition are listed.

FIB fabrication is complete, we use SerialEM[33] and CorRelator[7] to relocate the ROI based on fluorescent signals and perform MPACT ($m \times n$; for example, 3 × 3) acquisition. Automated tile sorting and montage stitching generate 10 tilt series (1 fully stitched montage and 9 (3 × 3) individual tile tilt series) in 1.5 h (Fig. 2; Steps 46–73) before tomogram reconstructions in IMOD-Etomo (Fig. 2; Steps 74–76). Alternatively, montaged tilt series can be stitched during the tilt series alignment and tomogram reconstruction in IMOD-Etomo[34]. Montage tomograms can be segmented in Thermo Scientific Amira 3D Software[35,36] (Thermo Fisher Scientific), EMAN2 (ref. 37, or Dragonfly[38] (Comet Technologies Canada Inc.; Fig. 2; Step 77). For computational efficiency, subtomograms can be extracted from individual tile tomograms, aligned and averaged—known as STA[39]—using Dynamo[40] or PEET packages[41], and then transferred to Relion[42] (Fig. 2; Step 77).

Level of expertise needed to implement the protocol

This protocol is based on the 2D cryo-CLEM[6] and conventional cryo-FIB milling procedures[43]. To use this protocol, scientists should be familiar with cryo-FLM, cryo-ET and cryo-FIB techniques and be comfortable with preparing and handling cellular samples, including cell culture, live-cell labeling, grid seeding, plunge freezing and grid transfer steps. In addition, scientists who follow this protocol to collect correlative MPACT data should become familiar with basic SerialEM operations, including setting up low-dose imaging mode and utilizing the navigator functions. It is worth noting that integrated FLM systems may vary due to differences in the availability and accessibility of instrumentation. The cryo-FLM and cryo-ET techniques applied may need to be adapted depending on the biological questions being explored. However, the single-pair transformation for 3D site-specific FIB fabrication, the batch acquisition of montage cryo-ET data via the MPACT scheme and the data processing routines for automated tile stitching and individual tile tilt series generation should be applicable to a broad range of 3D cryo-FLM-FIB-ET experiments on modern triple condenser lens life-science TEM systems with stable beam shifts and stage tilt holder (Autoloader systems).

Applications of the method

This protocol presents a robust 3D correlative iFLM-guided automated FIB-milling workflow for generating thin lamellae suitable for conventional cryo-ET or montage cryo-ET data acquisition via MPACT[26]. This method, or variations of it, has been successfully applied to neurites of primary *D. melanogaster* neurons[30], mitochondria associated with lipid droplets (LDs)[18] and rarely visualized objects such as centrosomes[18,19]. Valuable aspects of this protocol include a simplified single-pair 3D transformation between FLM and FIB-SEM, as well as automated FIB milling parameters applicable to many dual-beam systems equipped with an in-chamber FLM. We demonstrate that MPACT[26] can be easily implemented on existing modern triple condenser lens TEMs (stable stage and beam shifts) and integrated with other preparative techniques such as micro-patterning[30,31]. Compared with conventional single-tilt series cryo-ET data collection (20–25 min per tilt series acquisition), MPACT routinely produces ten usable tomograms (one fully stitched montage and nine individual tile tilt series) in 1.5 h. With the increasing demand for broad adoption and accessibility of high-throughput cryo-ET along with seamless data sorting and montage stitching, we anticipate that this protocol will be routinely used by the structural and cell biology research communities for in situ cryo-ET structural studies of common and rarely found macromolecular complexes in cryo-FIB thinned cellular lamellae.

Comparison with other methods

Targeted 3D correlative milling methods include fiducial-based or feature-based transformation using external CLEM instruments[9,10,14], commercial FIB-SEM instruments[8] or customized integrated FLM-FIB-SEM systems[18–20]. In some cases, higher-resolution FLM may be achieved; however, the time required to perform on-the-fly correlation without fully integrated software and automated workflows is prone to error, thus reducing success rates and throughput. In this iFLM module and protocol, a multiband filter set (Fig. 3d,e) is used for simultaneous and sequential imaging of multiple fluorophores, thereby eliminating the need for filter cube switching times and pixel shifts between individual filter sets. We compared single-band optical filter sets in the Leica Thunder cryo-CLEM with the multiband filter set of

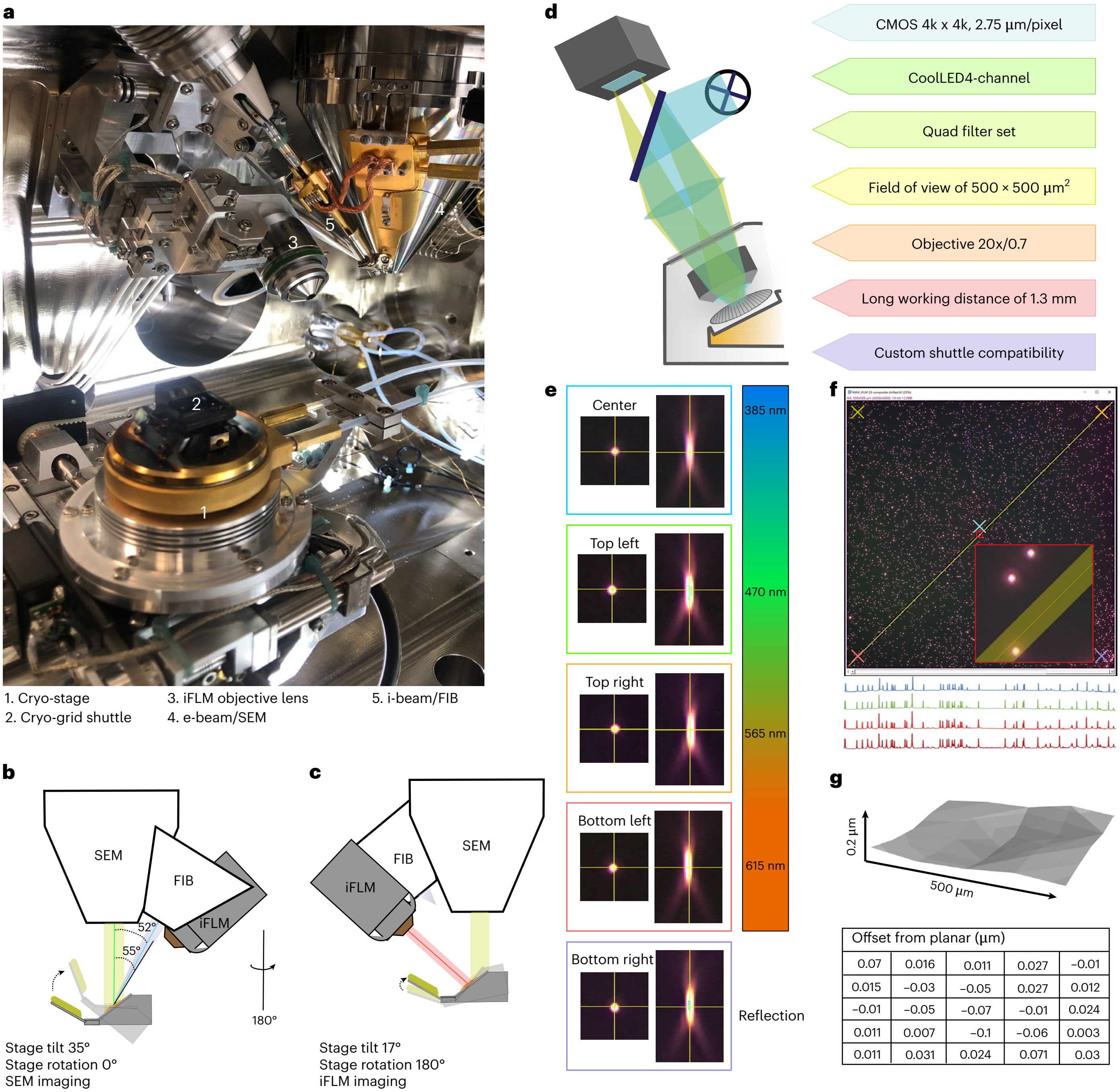

Offset from planar (µm)				
0.07	0.016	0.011	0.027	−0.01
0.015	−0.03	−0.05	0.027	0.012
−0.01	−0.05	−0.07	−0.01	0.024
0.011	0.007	−0.1	−0.06	0.003
0.011	0.031	0.024	0.071	0.03

Fig. 3 | Configuration of iFLM in a cryo-FIB-SEM Aquilos 2 system. a–**c**, The actual setup (**a**) and a schematic diagram (**b** and **c**) of the in-chamber overview of the iFLM relative to the FIB and SEM columns, and the stage/shuttle position in the cryo-FIB-SEM Aquilos 2 system (Thermo Fisher Scientific) from the front (**b**) and the back (**c**) chamber camera mounted in the back. The stage rotates 180°, moves laterally, tilts to where the fluorescence imaging angle is perpendicular to the grid surface for iFLM imaging (stage tilt of 17° with a 35° pre-tilt shuttle). The stage returns to the SEM imaging position where the SEM viewing angle is perpendicular to the grid surface (stage tilt of 35°) and milling position where the FIB is positioned at a shallow milling angle (stage tilt of 6° to 9°, corresponding milling angles of 9° to 12°). **d**, A simplified cartoon illustration outlines the iFLM beam paths and hardware features including camera and filter set. **e**–**g**, iFLM resolution performance in fluorescence and reflected light microscopy modes: the *xy* and *xz* central slices of the PSF for fluorescence and reflection channels in the iFLM quad filter set exhibit chromatic aberrations (**e**); flatness of the field of view under all fluorescence channels demonstrated by the brightness of the beads in contrast to the background along the diagonal line of 700 µm (**f**); curvature of the field of view under all four channels demonstrated by quantification of the *z*-offset of 200 nm TetraSpeck beads in 25 subfields of 100 × 100 µm², on a flat glass coverslip (**g**).

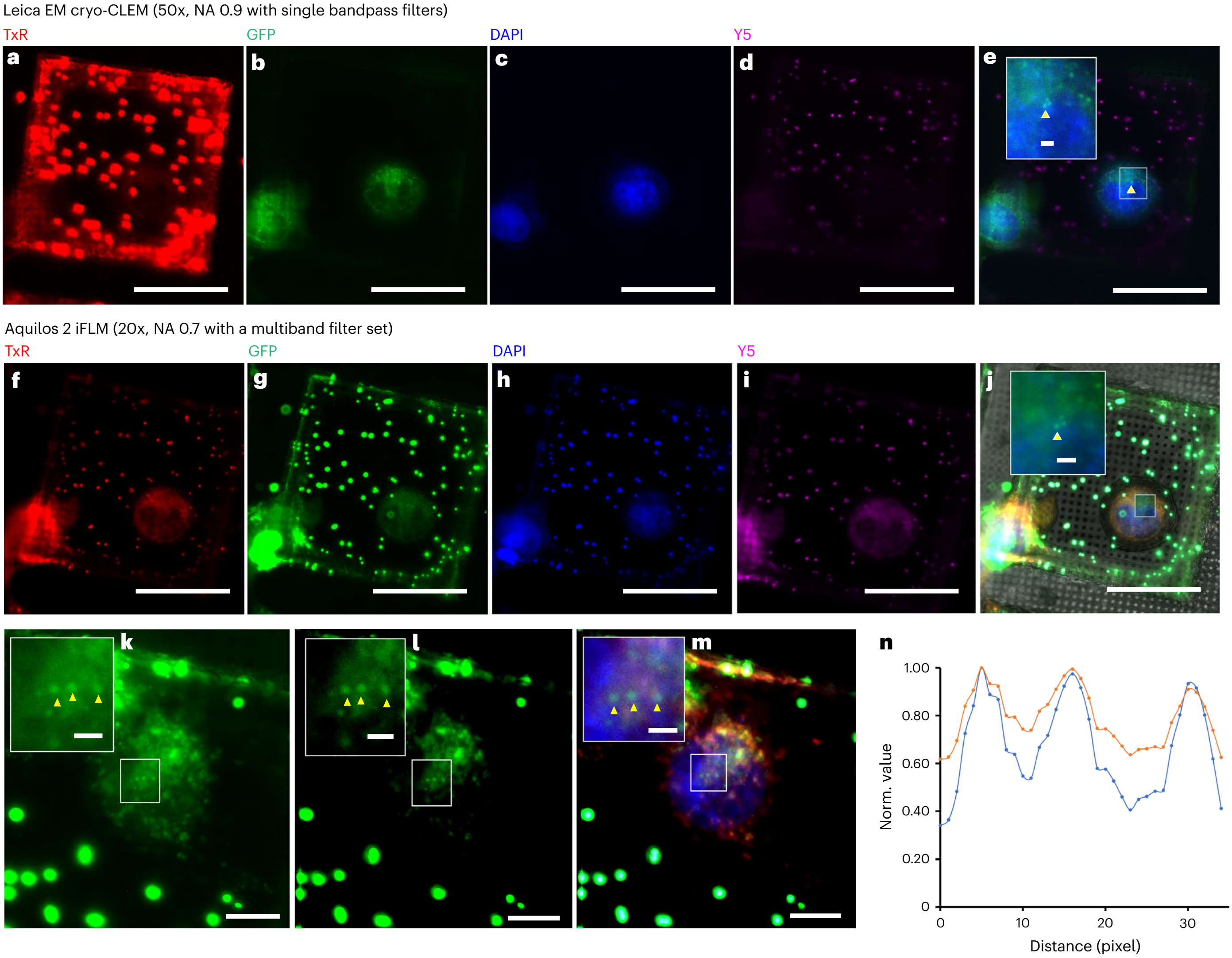

Fig. 4 | Transmittance performance and improved resolution of FLM imaging under cryogenic conditions. The cryogenic transmittance performance of multiple fluorescent signals was examined on the same grid using the same plunge-frozen HeLa cell with labeled mitochondria (red, MitoTracker, ex/em 581/644), lipid droplets (LDs, green, BODIPY, ex/em 493/503), nucleus (blue, Hoechst, ex/em 350/461) and an addition of external 1 µm FluoSpheres (ex/em 585/605) as registration markers. **a**–**e**, The single-band-pass filter cubes (TXR ex560/40 em630/76 (**a**); GFP ex470/40 em525/50 (**b**); DAPI ex350/50 em460/50 (**c**); Y5 ex620/60 em700/75 (**d**)) from a Leica THUNDER cryo-CLEM system. **f**–**j**, The multiband-pass filter (TXR ex560 (**f**); GFP ex470 (**g**); DAPI ex385 (**h**); Y5 ex625 (**i**)) performance of an iFLM-Aquilos 2. Both systems are equipped with ceramic objective lenses (NA of 0.9 in Leica cryo-CLEM and NA of 0.7 in iFLM-Aquilos 2) and room temperature (RT) CMOS-based detectors, operating in the wide-field mode with samples under cryogenic conditions. **a**–**d** and **f**–**i** are fluorescent signals from corresponding channels. **e** is the merged fluorescent channel view of **b**–**d**. **j** is the merged fluorescent channel view of **g**–**i** plus reflection. **k**–**n**, The resolution of iFLM images could be improved via conventional PSF-based deconvolution. The three green ROI (yellow arrowheads in **k**–**m**, BODIPY, ex/em 493/503) are shown in a single *z*-plane of a raw iFLM image (**k**), in the corresponding post-deconvoluted image (**l**) and in the deconvoluted merged multifluorescent image (**m**). **n**, Normalized (norm.) *x*-axis intensity plot file of the three ROIs in the raw (orange line) and deconvolved (blue) image plane shows undetectable pixel shifts after deconvolution processing, with clearly improved lateral PSFs of the ROIs (yellow arrowheads in **k**–**m**). Scale bar, 50 µm in **a**–**m** and 2 µm in the inset of **e**, **j** and **k**–**m**.

the iFLM module in the Aquilos 2 to evaluate performance, fluorescence bleed through and background noise (Fig. 4). With both filter options, we assessed artifacts associated with pixel shifts between color channels, unwanted fluorescence signal (Fig. 4a), prolonged imaging times and the adjustment of experimental procedures to reduce or eliminate these issues. Recently, a triple-coincident cryo-FLM-FIB-SEM system was developed, allowing for real-time FLM to be performed during FIB milling[19,44]. This configuration requires redesigning the cryogenic stage to enable simultaneous imaging of the sample from three angles by FLM, SEM and FIB. Consequently, the rotational range of the sample shuttle is limited to 28° of freedom at the coincidence point. In contrast, the rotational range of the sample shuttle is 54° with a perpendicular incidence point for iFLM and SEM imaging in an iFLM-equipped Aquilos 2 (Fig. 3a–c). The stage movement freedom and larger chamber volume of the Aquilos cryo-FIB-SEM also support the use of an Easylift needle for cryo-FIB Lift-out, which is essential for workflows associated with 'bulk' specimens such as tissue, organoids and organisms[45]. This iFLM arrangement is not exclusive to the Aquilos 2 system and can be incorporated into other commercialized cryo-FIB-SEM instruments, such as the Zeiss Crossbeam FIB-SEM[23]. In some cases, the point spread function (PSF) and resolution of iFLM modules are limited due to the physics of the wide-field imaging lens. However, improved contrast, information restoration and precise targeting (Fig. 3) can be enhanced by using deconvolution algorithms (Fig. 4k–m).

Linear transformations, such as affine transformations, are used for 2D coordinate transformations in cryo-CLEM applications[7,46–48]. A 3D rigid body transformation has been used for the superimposition of ROI from FLM to FIB for targeted cryo-FIB milling[9]. This approach required a set of well-spread, identifiable fiducials (in practice, $n > 10$) near the target region. In comparison, we established a more efficient linear transformation to extract *xy* coordinate information from the correlation between the SEM and iFLM. The *z* height coordinate data were derived by projecting 3D FLM information onto a 2D plane along the direction of the milling angle in the FIB view (Fig. 5). Instead of relying on direct localization, the *z* coordinate of the ROI is transformed based on its relative position to a single identifiable marker, detectable across all three (FLM, SEM, FIB) imaging modalities. The single ROI–marker method achieves target precision comparable to existing 3D rigid body transformation[9] (Fig. 5e) eliminating the requirement for iFLM and FIB overlays, suitable for various registration markers (Fig. 5d). In practice, we and others have reported an average of 80–85% of success rate of ROI retainment in final 100–250 nm lamellae from a wide range of samples (Table 1).

For montage cryo-ET, several strategies and hardware augmentations have been explored and used to minimize extra irradiation exposure to the sample; these include restricted beam sizes[49,50] and the replacement of the C2 aperture with a square aperture[51,52]. The use of a reduced beam size[49] and a hexagonal montage pattern produces even illumination across the sample; however, this arrayed pattern decreases tilt series collection throughput, requires a tile stitch scheme with substantial user intervention, and results in inflexible montage patterning. Insertion of a square C2 aperture appears promising for reducing unnecessary sample illumination and, combined with beam-image shift-based parallel cryo electron tomography[53], is capable of capturing large fields of view[51]. Nevertheless, this solution requires changes to the optical column of the microscope and adjustments to the microscope and camera alignments due to the insertion of the new aperture, as well as the elongation of the beam illumination perpendicularly to the tilt axis upon tilting[26,54]. While nonoverlapped tiled tilts may be stitched together[51], overlapping is still essential for producing a seamlessly blended tomogram. Stitching seams would otherwise appear in the blended tilt series and resultant tomograms. In addition, montage datasets collected without overlapping regions between adjacent tilt series tiles will require more user engagement during data processing.

In comparison (Table 2), MPACT[26] offers several key advantages. Already, stable TEM goniometers (for example, stages) combined with predictive solutions, such as fast-incremental single-exposure methods[55,56] and parallel beam-image shift acquisitions[53,54], have improved traditional cryo-ET data collection speeds by ~10-fold. Corrections for target tracking and applied defocus in conventional cryo-ET[33] are managed by acquiring tracking and focus images to estimate and correct for deviations caused by the mechanical tilting of the stage and sample. Depending on the tracking and focus scheme employed, this can be time consuming yet advantageous. In the end, the targets are well-preserved over the entire MPACT montage tilt series, and the defocus varies by ≤1 µm for each tile acquired at all tilt series angles. The use of beam-image shift to generate parallel arrays of illumination across a large field of view at each tilt has increased MPACT throughput by 3–4-fold. By moderately shifting the center of the tile pattern to spread the excessive dose in overlap zones, MPACT employs a regular array instead of a hexagon-packed tile scheme. While this approach is less efficient in terms of dose distribution

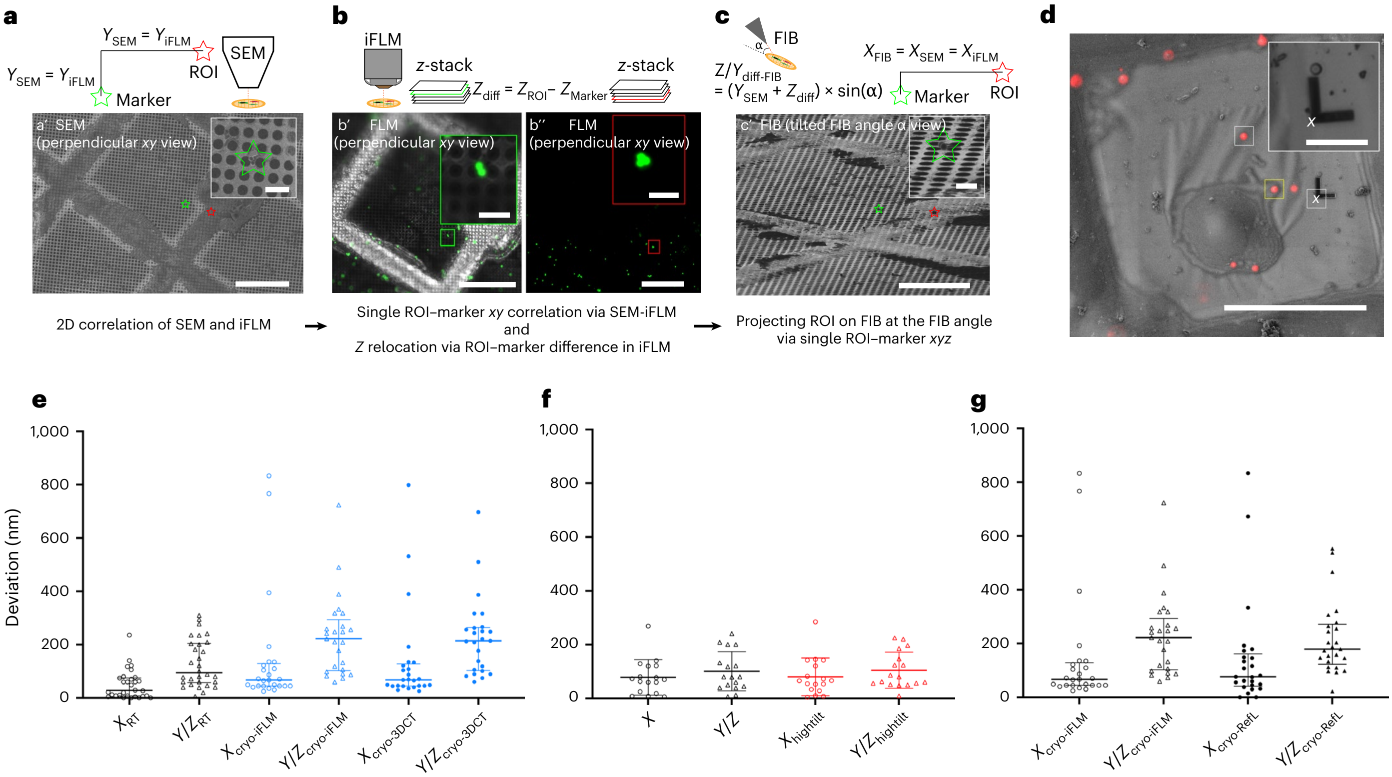

Fig. 5 | Coordinate-based single ROI–marker pair 3D correlation in an iFLM-FIB-SEM system. a–**c**, Single-pair ROI–marker registration of iFLM and SEM and its correlation projection on the FIB view to locate the ROI. Schematic diagrams (**a**–**c**) and corresponding data images (**a**′–**c**′) are shown to illustrate the process. The configuration of SEM and iFLM objectives enables a perpendicular projection (**a**) of the sample onto the shuttle, ensuring that the lateral location in *x* is equivalent across iFLM, SEM, and FIB after correlation between SEM and iFLM. The *z*-positioning takes into consideration the milling angle (α) and the actual *z* height difference between the ROI and the marker provided by the 3D iFLM *z* stack (**b**, FLM images, left: the *z* plane for the marker in focus, and right: the *z* plane for the ROI in focus). The 3D ROI relocation in *xyz* is achieved in the FIB view using single ROI–marker registration (**c**), where the *y* coordinate represents the 3D *z*-positioning information. **d**, A 1 µm FluoSphere bead (white box) serves as a fiducial marker point. The sharp corner of an L-shaped FIB-milled pattern (white box with an asterisk indicating the selected corner) on the support film within the same grid square could serve as an alternative fiducial marker for the fiducial ROI (yellow box) to perform marker registration/transformation. **e**, Targeting precision of the direct, unsupervised ROI localization for 1 µm FluoSpheres (em 605) under RT (*n* = 30, black data points) and cryo-conditions (*n* = 25, blue data points) in *x* and *y*/*z* (mean ± s.d.). The relocation precision in cryo-condition using the same data was performed in 3DCT. **f**, Precision of the targeting ROI location under RT of the same FluoSpheres (*n* = 17) (em 605) in *X* and *y*/*z* (mean ± s.d.) in shallow milling angle (9°, black data points) and high milling angle (21°, red data points). **g**, Targeting precision comparison of the same sets (*n* = 25) of FluoSphere as the ROI using either nearby 1 µm FluoSpheres in the fluorescence channel or the sharp corner of a L-shaped milled pattern in the reflection mode under the cryogenic conditions in *x* and *y*/*z* (mean ± s.d.). A known FluoSphere is used as the ROI to serve as the ground truth, and a nearby FluoSphere is selected as the marker for registration in **e**–**g**. Scale bars, 5 µm in **a**–**c**, 50 µm in **a**–**c** and **d**, and 10 µm in **d** (inset).

compared with other methods[51], it supports seamless montage blending with minimal user input and, most importantly, ensures ROI retention within individual tile tilt series, allowing for their independent reconstruction for subsequent STA analysis. Additionally, particle sorting based on dose exposure can be performed to exclude overdosed particles, enhancing the final resolution of the STA particle structure. Notably, MPACT is compatible with both fringe-free and non-fringe-free TEM systems, accommodates square or rectangular detectors and requires no mechanical alterations to the TEM. Nevertheless, the parallel beam illumination and montage tile overlaps implemented in MPACT benefit significantly from the triple condenser lens setup, well-calibrated beam image shifts and stable microscope stage. Setting up and using MPACT with a double-lens side-entry holder TEM system could be challenging.

Limitations of the protocol

The iFLM in the Aquilos 2 cryo-dual beam FIB-SEM is a wide-field microscope equipped with a 20× magnification lens, featuring an optional digital zoom up to 80×. To comprehensively

Table 1 | Success rates of single-pair ROI–marker registration with iFLM-MAPS-AutoTEM 2.4

Targets	ROI size	Lamellae sites	ROI retention	Marker
Lipid droplets (HeLa)	~500 nm	20	18	Microspheres
Mitochondria (HeLa/A549)	500 nm to 1 µm	25	20	Microspheres and/or sharp corner of a milling pattern
Actin bundles (HeLa)	2–5 µm in length (*xy*), 350–500 nm in *z*	10	7	Microspheres and/or flat ice chunks
Nucleolar proteins (yeast)	1–1.5 µm	40	37	Flat ice chunks
Lysosomes (neurons)	~500 nm	22	18	Flat ice chunks

Table 2 | Montage acquisition scheme comparison

Montage acquisition scheme	Dose efficiency	Hardware modification (compatibility)	Post-acquisition montage stitching	Single-tilt applicability	STA application	Reference
Square beam aperture + PACE	No tile overlaps	Yes (square C2 aperture, three-lens TEM systems)	Scripting that usually requires some user intervention, patchy tomograms	Yes	–	Chua et al.[51]
Montage Cryo-ET (Hexagon)	Minimal tile overlaps	No (fringe-free, three-lens TEM systems)	Scripting that usually requires some user intervention, smooth tomograms	No	–	Peck et al.[49]
MPACT	Moderate tile overlaps	No (suitable for both fringe-free and non-fringe-free, three-lens TEM systems)	Automated scripting that requires little user intervention, smooth tomograms	Yes	Yes	Yang et al.[26]

validate the performance of the iFLM module, we measured the PSF of 200-nm TetraSpeck fluorescent beads. On this system, the full-width half-maximum of the PSF is 410 and 1600 nm for the *xy* and *z* directions, respectively (470/510 nm channel). The field curvature aberration introduced by the iFLM objective lens had a nominal planar offset variation of 0.2 µm (Fig. 3f). During imaging, iFLM fluorescence image stacks could be further processed using standard deconvolution algorithms (Fig. 4l,m), which are suitable for the localization of ROIs above 500 nm. The smaller the ROI, the better the signal-to-noise ratio (that is, a brighter signal and less background noise) the iFLM needs for identification. It should be noted that due to the intrinsic lack of axial information in wide-field imaging, precise pinpointing of small ROI (<300 nm in *xyz*) to support cryo-FIB machining of 100–200 nm ROI-preserving lamella may be difficult. The inclusion of a confocal microscope in the FIB-SEM could be a solution. However, this configuration[18,19] is not yet commercially available. External cryo-confocal imaging remains an option before cryo-FIB milling (Fig. 2; Step 12). Based on our experience with a cryogenic objective (50×, NA 0.9, Leica) and a previous report using a long working distance objective (100×, NA 0.75, ZEISS)[57], commercial cryo-confocal systems can achieve resolutions of 250–400 nm in *xy* and 1–1.2 µm in *z* in practice.

Cryo-FIB milling of frozen-hydrated materials introduces internal stress points to lamellae, causing deformations that may alter the *z* heights of the ROI[16]. This can be monitored by iFLM imaging during FIB milling. Real-time iFLM imaging and two rounds of ROI refinement during FIB milling are described and recommended in this protocol; however, it requires periodic adjustments to the stage shuttle position for both FIB milling and iFLM imaging. Care should be taken because this process may introduce stage relocation and repositioning errors that can impact correlation (Figs. 1c and 3a–c).

The present protocol focuses on well-vitrified, plunge-frozen cellular samples that are less than 20 µm thick[58]. This type of grid will have a clear definition of grid bars and the cell sample embedded in a thin film of buffer visible by cryo-SEM (Fig. 6g). This type of sample and grid provides a scientist with clear and unambiguous marker options for single-pair ROI–marker 3D FLM to SEM to FIB transformations necessary for targeted FIB-milling. High-pressure freezing is highly recommended for preserving isolated organelles, cells, and tissue samples of ~50–200 µm thickness[59]. High-pressure frozen samples will be embedded in a smooth, flat slab of ice with no visible surface topography. In this case, single-pair ROI–marker 3D linear transformations may

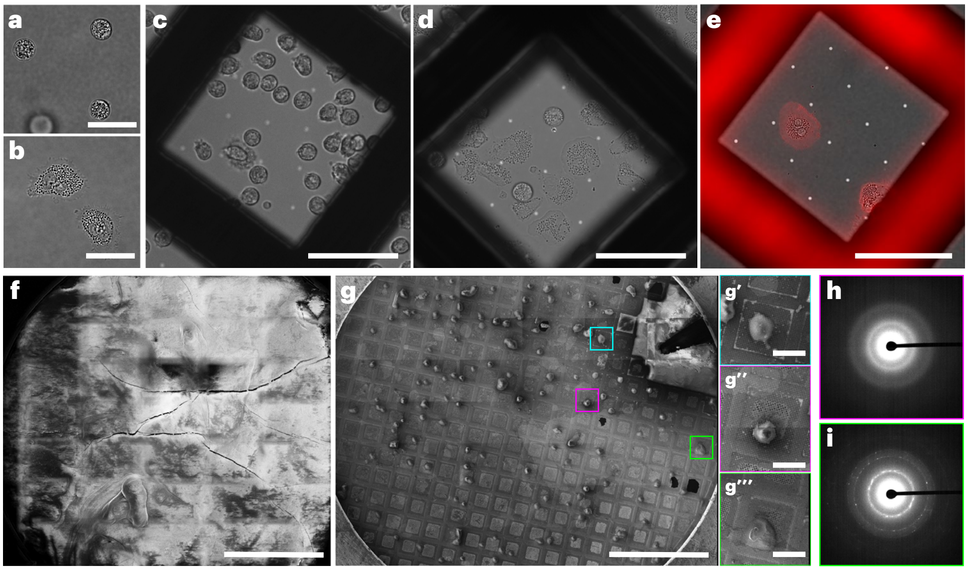

Fig. 6 | Grid optimization and vitrification. a–**e**, The steps followed to optimize sample preparation before freezing, using the activation of human EOS as an example, via live-cell wide-field imaging: EOS adheres to and spreads across the glass surface, changing from a spherical shape (**a**, 10 µm in height) in its non-activated state to a thin pancake-like morphology (**b**, up to 1 µm in height), upon IL-33 activation. Without proper grid surface treatments, EOS does not respond to activation and will not adhere to the support grid foil (**c**). Glow discharging, 70% ethanol washing and extracellular matrix coating ensure consistent activation of EOS cells on the foil (**d**). The cell density per square is optimized to achieve 1–2 cells per square (**e**), as too many cells (**d**) cause insufficient blotting during the plunge freezing. Activated EOS are stained with a low toxicity membrane dye (ex/em 656/676 nm) to visualize the thin cell membrane boundary (**e**). **f**–**i**, Vitrification assessment using cryo-SEM and TEM diffraction. Upon loading into the cryo-FIB-SEM dual-beam system, an SEM grid overview quickly assesses sample vitrification and millability for the production of 200 nm lamellae: insufficient blotting (**f**) usually results in solid chunks of ice on the surface, which are unsuitable for FIB fabrication. Well-frozen adhesive mammalian cells on the grid show clearly defined grid bars, foil and cell shapes (**g**). Within the same grid, some areas have better vitrification (inset, **g′**, cyan) where the mesh holes are visible, compared to thicker ice areas (inset, **g″**–**g‴**, pink and green). Cell clusters (inset, **g‴**, green) are prone to thicker ice and insufficient vitrification, making them less ideal for thin lamellae generation. Under TEM, electron diffraction is used to assess and confirm the presence of amorphous ice (**h**) that has smooth, diffuse rings versus diffraction from crystalline ice (**i**) present in various regions of one or more lamellae. Scale bars, 20 µm in **a** and **b**, 50 µm in **c**–**e** and insets in **g** and 500 µm in **f** and **g**.

be more challenging to apply unless predefined markers (for example, pre-etched patterns) can be accurately identified on the ice slab surface[60].

Currently, the iFLM-guided live 3D targeted milling remains a semi-automated process, requiring user intervention for fluorescent image stack acquisition, image deconvolution, single-pair ROI–marker registration in MAPS and relocalization of the marker in AutoTEM. More automation and multifunctional software programs (for example, on-the-fly deconvolution) are under development.

Experimental design

Sample preparation: choice of cell types, grid preparation, live cell imaging

The selection of grid substrates is crucial for maintaining cell viability throughout the sample preparation steps in the workflow[6]. Gold (Au) EM grids are commonly used because copper (Cu) grids are toxic to cells. A range of rigid and stable support films is available, and some may be more suitable than others for cryo-FIB fabrication[22,61]. We have found that SiO_2-foiled 200-mesh Au-Quantifoil grids function well for most adherent and nonadherent cell types. The selection of Quantifoil hole size and spacing is sample dependent. For primary cells, such as neurons[30] and EOS[29], we commonly use R1.2/20 grids with 1.2 µm hole diameters spaced 20 µm apart (Fig. 6c–e). For immortalized cell lines and bacterial cells, such as HeLa cells, fibroblasts and *E. coli*, we regularly use R2/1 grids with 2 µm hole diameters spaced 1 µm apart[6,31,32]. Live-cell staining or label introduction is performed before vitrification (Figs. 4 and 7). We also recommend live-cell FLM imaging of the on-grid cultured cells before freezing (Fig. 1). Note that the FLM coordinates may change between live-cell FLM and vitrification. Nevertheless, live-cell FLM can capture higher-resolution information and serves as a last check for sample integrity and cell structure preservation.

Sample vitrification: freezing apparatus, use of cryo-protectants, and fiducial application

Back-side or single-side blotting is highly recommended when plunge-freezing eukaryotic cells[43,62]. Here, we describe the parameters used with a Leica EMGP (either model 1 or 2). Detailed step-by-step freezing protocols using a Leica EMGP (1 or 2) have been described previously[63]. Other plunge freezing systems can also be used as well[6]. Here, we focus on glycerol incubation and the application of FluoSpheres during the freezing of mammalian cells. In practice, we and others have observed regions of insufficient vitrification in plunge-frozen cultured cells up to 10–15 µm thick (Fig. 6g). Crystalline ice (Fig. 6i) from poor vitrification damages cell structure and reduces the quality of tilt series and tilt series alignment because of the presence of Bragg reflection patterns[62]. With several cell types, we routinely incubate the on-grid cultured cells in a cryoprotective solution of 10% glycerol (commonly 1× DPBS or PBS) before plunge-freezing (Fig. 6g,h). A ~5 min 10% glycerol incubation is sufficient for proper vitrification of eukaryotic cells <20 µm thick. Routine fluorescence microscopy can be used to assess cell thickness. Glycerol and glycerol derivatives are present in cells, and their presence has not precluded high-resolution structure determination. However, the addition of glycerol (up to 40–60% wt/wt) to the sample media may increase the baseline fluorescence signal by altering the behavior of the dye molecule[64,65]. Second, the addition of ~50% glycerol to cryo-EM samples has been shown to increase beam-induced motion and sample sensitivity to radiation damage[66]. Nevertheless, macromolecules suspended in 20% glycerol solutions have been used for high-resolution single-particle analysis structure determination[67]. We have not experienced significant negative impacts reported for higher glycerol concentrations when using a cryo-protective glycerol concentration of 10% (refs. 66,67), although we have seen some increased sensitivity to electron dose. A well-vitrified plunge-frozen grid of cells exhibits visible grid bars, holes in the foil and cellular 'mounds' (Fig. 6g'). We recommend the addition of 1 µm FluoSpheres and the use of FIB-etched patterns (Fig. 5d) as fiducial markers. The FluoSpheres are readily identified in FLM, FIB and SEM live views and images, making them ideal markers. The fluorescent signal of FluoSpheres is strong and may exhibit autofluorescence when imaged under cryo-conditions (Fig. 4). We optimize the concentration of FluoSpheres to achieve 10–15 beads per grid square, taking advantage of the autofluorescence to minimize chromatic aberration-induced pixel shifts that occur at different emission wavelengths.

Cryo-iFLM-FIB-SEM instrument

FIB-milling with an Aquilos 1 cryo-FIB-SEM has been reported previously[43]. In this protocol, we focus on the iFLM instrument configuration. The principal design of the iFLM for the Aquilos 2 cryo-FIB-SEM system was for the FLM objective and the FIB-SEM probe-forming lens to maintain suitable working distances to support all imaging modalities and ROI relocation between the two imaging positions. In the main vacuum chamber of the Aquilos, the FLM objective is positioned parallel to the FIB column (Fig. 3a,b). The stage can be moved laterally, be reoriented, rotated and tilted to accommodate iFLM, SEM and FIB imaging or FIB-milling (Fig. 3a–c). To support the three modes of operation, the iFLM-Aquilos 2 shuttle has a pre-tilt of 55° between the EM grid and e-beam surface (35° between the EM grid and stage surface) (Fig. 3b,c). The iFLM module and its location in the instrument chamber have several advantages: (1) retention of a perpendicular (90°) incidence point to the sample surface to support the application of an affine transform for correlation between the FLM and SEM, and the FLM and FIB; (2) a longer working distance of 1.3 mm for the FLM, compared with 1 mm; and (3) a piezoelectric positioner for focusing the FLM. The iFLM objective lens is an 20× Zeiss Epiplan-Apochromat objective lens with an NA of 0.7, a field of view of 500 × 500 µm^2 per frame, with an unbinned image pixel size of 0.125 µm at 20× magnification, and high-vacuum compatibility (Fig. 3d). To minimize pixel shifts between individual filter sets (Fig. 4a–e) and the time required to switch filter cubes, a multiband filter set (Fig. 4f–j) is used for simultaneous and sequential imaging of multiple fluorophores, this is coupled with a CoolLED light source and room-temperature (RT, 20–22°) 4K × 4K CMOS camera (Fig. 3d). The use of a standard CMOS camera eliminates possible light microscopy (LM) image blurring from internal vibration and permits larger pixel densities not typically found with sCMOS. This supports digital magnification changes between low and high magnifications (40× and 80×), which have been incorporated in iFLM v. 1.4.0 and above, and efficient navigation across a larger field. In addition to four fluorescence channels, bright-field imaging is supported by reflected light illumination.

There are several considerations for optimal cryo-FLM image quality that impact registration and transformation:

1. We recommend testing cryo-FLM imaging parameters including different iFLM filters to determine which perform the best. Fluorophores at cryogenic temperature undergo changes[64] such as extended triplet state duration, reduced photobleaching, spectral shifts, and lowered photon capture. Most assessments of fluorophore properties are conducted at room temperature.
2. In general, Nyquist sampling rates in the axial (z) plane of 2.5 to 3 times (1/2.5 or 1/3) the minimum resolved distance d are used. Per Abbe's diffraction formula $d_{xy} = \frac{\lambda}{2\mathrm{NA}}$ and $d_z = \frac{2\lambda}{\mathrm{NA}^2}$, the iFLM objective has a theoretical resolving power of 275 nm in lateral xy plane and 1.5 µm in the z direction, where λ is 385 nm and NA = 0.7 (dry). In practice, we use the sampling rate of 350 nm to collect z stacks.
3. High-intensity FLM exposures can devitrify cryo-samples. We recommend using lower intensities and longer exposure times to collect a sufficient FLM signal. Our recommendation for adjusting the intensity is to use a maximum of 35% of the full (wavelength dependent) illumination power at the exit pupil of the NA = 0.7 objective lens. The maximum irradiance (100% full illumination power) measured at the exit pupil was 4.55, 1.19, 1.83 and 1.78 W/cm^2 for 385 nm, 470 nm, 656 nm and 625 nm, respectively.

Correlation between iFLM and SEM and FIB: 3D correlation algorithm and FIB milling box positioning

We use the single ROI–marker coordinate registration strategy to correlate position and image data in the iFLM-Aquilos 2. This approach applies a 2D affine transformation to first correlate SEM and FLM images, transferring the ROI coordinates from the iFLM to the SEM in the xy plane (Fig. 5a). Using a linear transformation, SEM and iFLM images that contain the ROI coordinate information are projected onto FIB images acquired at the milling angles where the y coordinate represented both translation in y in the 2D xy plane and the z height information in the 3D projection (Fig. 5a–c). Instead of directly using ROI coordinates for transformation, a fiducial marker identifiable by both SEM and FIB is used (Fig. 5b). Then, the ROI can be projected onto the FIB view using its relative position to the fiducial marker. The z location of the ROI relative to the marker is represented in the y direction of the projected view (Fig. 5c). This approach does not superimpose FLM-SEM on FIB for coordinate prediction and transformation, simplifying the 3D correlation process. Following classic leave-one-out methods, we measured the relocation precision of the transformations by assigning one FluoSphere as an ROI (for example, ground truth) and another as fiducial marker (Fig. 5e–g). The relocation precision of the FluoSpheres at either RT or cryogenic temperatures is within 100 nm in x (xy, lateral) and 150 nm in y (z positioning), comparable to the 3D rigid body transformation known as 3DCT[9] (Fig. 5e). While deconvolution improves the image quality, the target precision comparison (Fig. 5) performed in this study utilized raw, unprocessed iFLM images to demonstrate the workflow's robustness.

There are a few critical features of the transformation:

1. The single-pair ROI–marker registration correlation strategy is based on decomposed xy and z linear transformations. Specifically, in 2D plane projections, the SEM and FIB have the same coordinate information in the x direction.

$$X_{\mathrm{SEM}} = X_{\mathrm{iFLM}} = X_{\mathrm{FIB}},\ Y_{\mathrm{SEM}} = Y_{\mathrm{iFLM}}$$

Therefore, the points identified in iFLM can be directly transferred from iFLM-SEM to FIB after the initial iFLM to SEM correlation. To correctly transform a non-flat 3D object from iFLM to FIB, for example, biological samples, the z-height information of the object relative to the support xy plane surface needs to be incorporated. It is implicitly understood that the Y_{FIB} coordinate represents both the xy 2D plane and the 3D z-height information related to the 2D projection of the ROI. In practice, we found that the relative positioning of ROI to a nearby 'fiducial marker' object, relative xy and a height difference in z, could serve as one unambiguous registration point. This offers an advantage over direct ROI coordinate correlation where multiple registration points ($n \geq 5$) need to be well-spread for accurate transformation calculations[9]. By identifying a single Marker point and its Z/Y_{FIB}, we could locate the ROI, based on the relative difference in z between ROI and marker. Here, with α as the milling angle, this yields,

$$Y_{\mathrm{diff-FIB}} = (Y_{\mathrm{SEM}} + Z_{\mathrm{diff}}) \times \sin\alpha,\ Z_{\mathrm{diff}} = Z_{\mathrm{ROI}} - Z_{\mathrm{Marker}}$$

2. Previously, we and others[7,46] showed that both closed-form least square linear transformation and nonlinear algorithms such as nonrigid thin plate spline work well for plunge-frozen grids when little deformative artifacts or geometric distortions are present. However, it is advisable to select points within the same square and close to the ROI. Some minor nonlinear deformation might still be expected across different regions on the grid.
3. The target precision of the single-pair ROI–marker method is independent of milling angles used (Fig. 5f).
4. The single marker could be a FluoSphere, a grid bar corner, an ice particle or an FIB-etched milling pattern. We examined the use of milled reference patterns, such as an 'L' (Fig. 5d), as a marker because they could be identified in iFLM reflection and FIB imaging modes. Similarly[18], the relocation precision of milled fiducial markers imaged under reflection mode was comparable to FluoSphere-based registration under the FLM mode (Fig. 5g). If nonbead features or reflection mode signals are chosen as the marker, it is important to ensure its precise relocation in the FIB view. The identified z height of the marker in the FIB view needs to match the z information obtained from its iFLM image stacks.

Correlative automated FIB milling procedure

While several steps in the correlative targeted milling workflow are semi-automated as noted (Fig. 2), Thermo Scientific MAPS Software 3.21 (and above) and Thermo Scientific AutoTEM Cryo 2.4 (and above) functions perform all calculations and correlations, including the 2D linear transformation between SEM and iFLM, relative z height determination, identification of single-pair ROI–markers and subsequent transformations between image coordinates and real-time stage positions. This 3D correlative workflow is well integrated into the automated FIB-milling process.

As discussed here and previously[15,16], cryo-FIB milling of frozen samples introduces internal stresses and deformations to lamellae, which may result in changes to ROI z heights. We examined this by monitoring mechanical drift through the tracking of distinct sample structures during milling. We observed 50–400 nm shifts in the xy direction surrounding milled lamellae (Fig. 7). To precisely locate and preserve ROI all the way through, single-pair ROI–marker correlations were applied twice. The first correlation guides the placement of the milling pattern on the intact target to produce a 1.5-µm-thick lamella at the end of the rough milling stage (Figs. 1, 8a–e and 9a–c). Then, the finer milling patterns are adjusted from the second round of iFLM-SEM-FIB correlation on the 1.5-µm-thick lamella 'chunk' (Figs. 8f,g and 9e–g). With this two-stage correlation approach, automated milling and polishing can reliably generate ~200-nm-thick lamellae that preserve the ROI (0.5–1 µm in thickness). Another consideration[17] is the linear thermal expansion coefficient of the supporting materials, where alternative mesh, foil and spacing options (such as titanium grids with 1/20 spacing) could be explored to mitigate local movements[22]. A final iFLM image is then acquired for FIB-to-TEM-to-cryo-ET correlation (Figs. 1, 8h,j and 9i).

Correlative cryo-ET imaging: MPACT batch setup for improved automation

Once a grid is transferred to TEM, using SerialEM[33], a low-magnification image or a montage of medium-magnification images is acquired of the entire lamella. It is used to correlate with

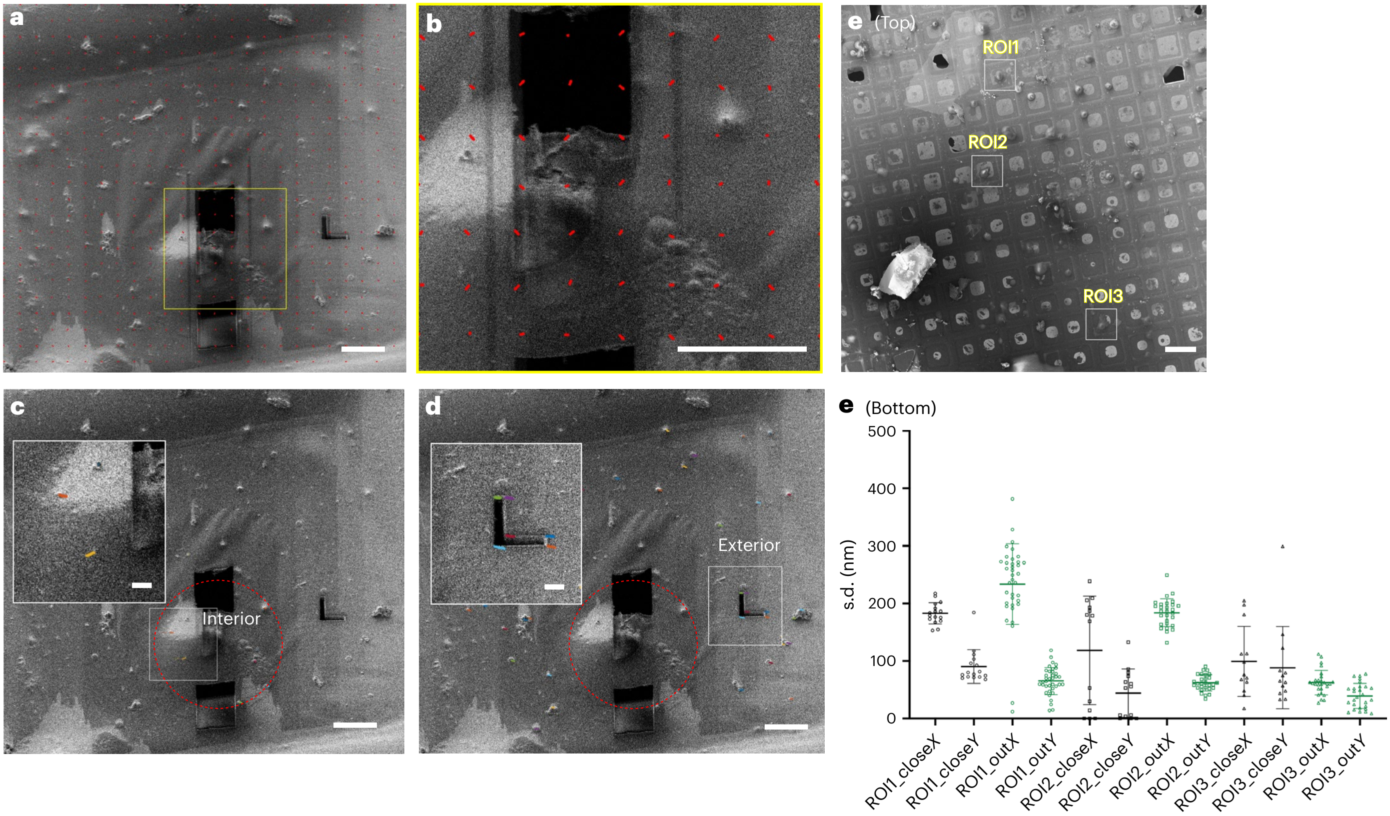

Fig. 7 | Movement of fiducial markers during cryo-FIB milling. a, A larger field of view to show the lamella ROI milling site and L-shaped marker for the measurement of the global movement of the objects. **b**, A zoomed-in view of the yellow boxed region in (**a**) where the red arrows (located in subregions with dimensions of 0.5 × 0.5 μm^2) indicate global movements of the milling site. **c**,**d**, The local movement of the objects/landmarks during the lamella milling process (**c**, interior, 16 μm in radius, red circle, inset: a zoomed-in view of the white boxed region) and the outer region (**d**, exterior, inset: a zoomed-in view of the white boxed region). Each color line represents a moving trajectory of a landmark during the milling the process. **e**, Quantitative analysis (bottom) of the movements of three frozen mammalian ROI milling sites on a representative grid (top) via tracking the interior and exterior landmarks throughout the entire FIB milling process. The movement is presented via the s.d. of the coordinate in *x* and *y* of the landmark (mean of measured s.d. ± s.d. of measured s.d.). Larger s.d. indicates larger movements of the landmark. Scale bars, 10 μm in **a**–**d**, 1 μm in **c** and **d** (inset) and 100 μm in **e** (top).

the final iFLM image of the ~200-nm-thick lamella (Steps 46–58; Figs. 2, 8i,j and 9h,i). Our group uses CorRelator[7] to directly transform cryo-iFLM coordinates into TEM stage positions, generating live Navigator files and FLM-TEM image overlays to identify fluorescent ROI (Figs. 8j and 9i). Alternatively, MAPS software can be used for offline correlation to produce a FLM-TEM image overlay, informing the manual selection of sites in SerialEM. The medium magnification view is then collected at the desired ROI site to serve as the 'Target Map' for the stage to return and realign to during regular batch tilt series acquisitions.

The decision to implement regular single-tilt series versus montage acquisition largely depends on the experimental goals and ROI. MPACT is particularly useful when seamlessly stitching 3D information at high magnification (pixel size between 2.5 and 5 Å) of a larger field of view (FOV) is required for data analysis, such as cytoskeleton growth and organization in primary neurites[30]. MPACT also maximizes the acquisition of content when biological ROIs are densely packed[68] and obtaining 3D information of each one is crucial in understanding cellular activities. For example, we needed to retrieve both reciprocal (micro-ED) and real-space (cryo-ET) data of secretory granules within primary human EOS cells, combined with their cellular context to understand how structural changes correlate with degranulation mechanisms[29]. While MPACT enables routine STA processing via utilization of subtile tilt series,

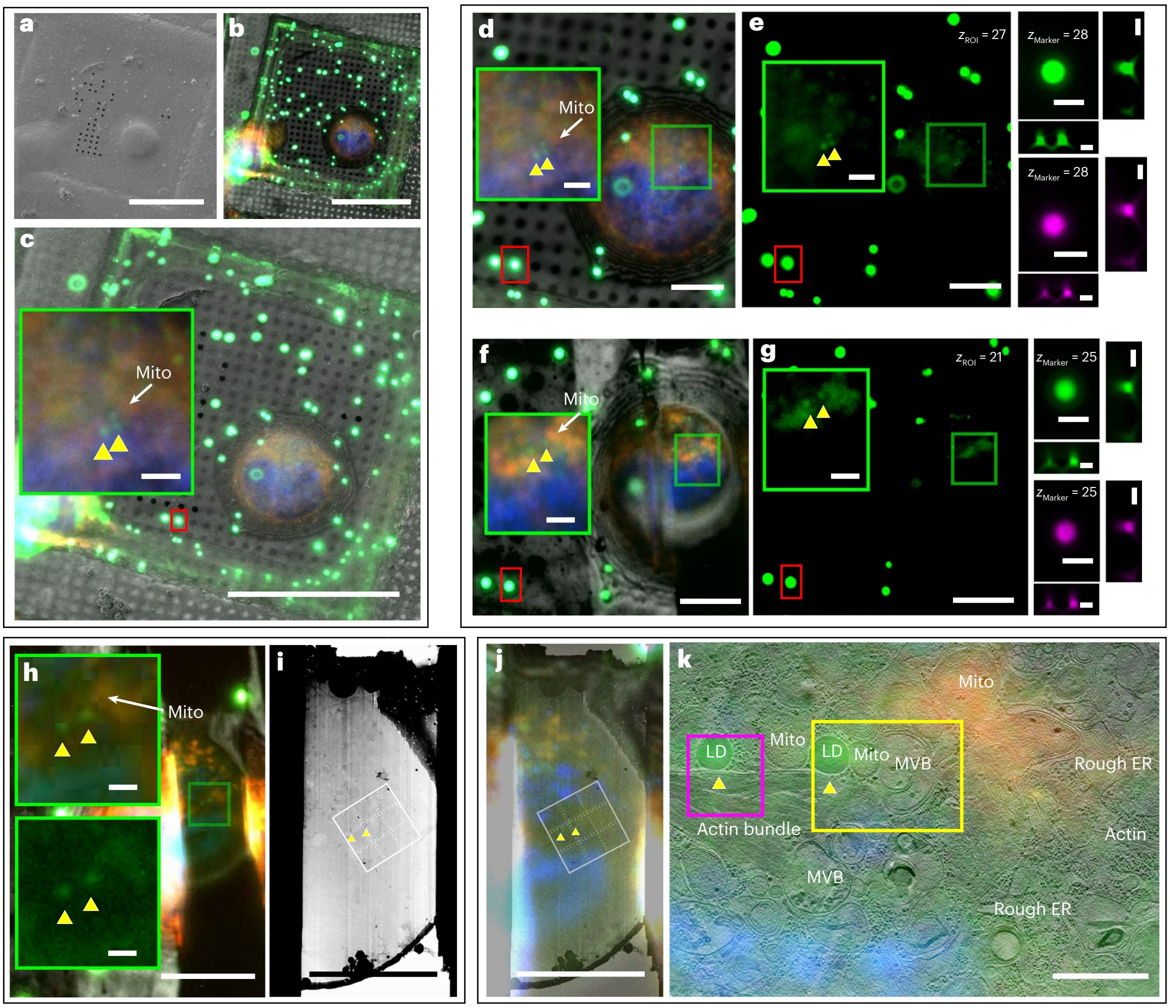

Fig. 8 | Representative results of iFLM-guided FIB-milling and MPACT of HeLa cells to study LD–mitochondrial contact sites. **a**–**c**, The initial 2D *xy* correlation: the 2D XY-correlation of SEM (**a**) and iFLM (**b**) of a HeLa cell with labeling of lipid droplets (LDs, green), mitochondria (red) and nucleus (blue) showed two adjacent LD (yellow arrowheads) next to mitochondria (white arrow) as ROI in the overlay (**c**) (Step 1). The FluoSphere beads are 1 µm in diameter (ex/em 585/605). **d**,**e**, Single-pair ROI–marker *xyz* registration: two rounds of 3D targeting are achieved via the single-pair ROI–marker transformation. The merged fluorescent channel image (**d**) shows that the target LD pair (ROI, yellow arrowheads) and nearby FluoSphere (marker, red boxed) both exhibit the green signal due to the iFLM multiband-pass filter. Initial targeting was performed (**e**) using the *z*-stack plane differences between the ROI (*z*-slice = 27 for the ROI in the iFLM stack of the unmilled cell, green box) and the marker (*z*-slice = 28 for the marker, red box) (Step 2). No discernible chromatic shifts nor aberrations were observed for the GFP ex470 and Y5 ex625 signals (**e**, right), suggesting that the marker *z* plane can be extracted from the ROI green channel. **f**,**g**, The second round was performed after rough milling using the *z*-plane difference obtained from the iFLM image stack of a 3-µm-thick lamella chunk (*z*-slice = 21 for ROI and *z*-slice = 25 for the marker). **f**, A merged channel view of the ROI and marker. **g**, Individual channel views of the ROI and marker at their corresponding *z* planes without discernible chromatic aberration. **h**, ROI relocalization in TEM: the subsequent automated milling proceeds to the ~200 nm lamella without interruption (Step 3). The final iFLM images (top, all channel overlays and bottom, green/GFP channel only in **h**) of the 200 nm lamella show the preservation of two original LD ROI (yellow arrowheads) as in **c**–**g**, **i**, **j** and **k**. **i**,**j**, MPACT acquisition and processing: the TEM image alone (**i**) and overlay of iFLM and TEM images of the 200 nm lamella (**j**) show the preservation of the ROI (yellow arrowheads) for cryo-ET tilt series collection (Step 4). The orientation of the white 3 × 3 box matched with the 3 × 3 cryo-ET montage acquisition via MPACT of the lamella's orientation on the microscope stage. **k**, Superimposition of the iFLM image and the reconstructed 3 × 3 cryo-ET montage. Each main step (1–4) is boxed in black. MVB, multivesicular bodies; ER, endoplasmic reticulum; Mito, mitochondria; LD, lipid droplets. Scale bars, 50 µm in **a**–**c**, 10 µm in **d**–**g**, 2 µm in *xz* and *yz* views of the same marker beads before the milling (**e**) and after the rough milling (**g**) and insets in **d**–**h**, and 1 µm in **k**.

removing particles within the overlap zones proves to be necessary to achieve better resolution in the averages. This inevitably decreases the particle copy numbers and could be challenging to implement when the ROI is already sparce in situ[24]. Therefore, we recommend single-tilt series when in situ high-resolution structural determination of sparce macromolecules is the

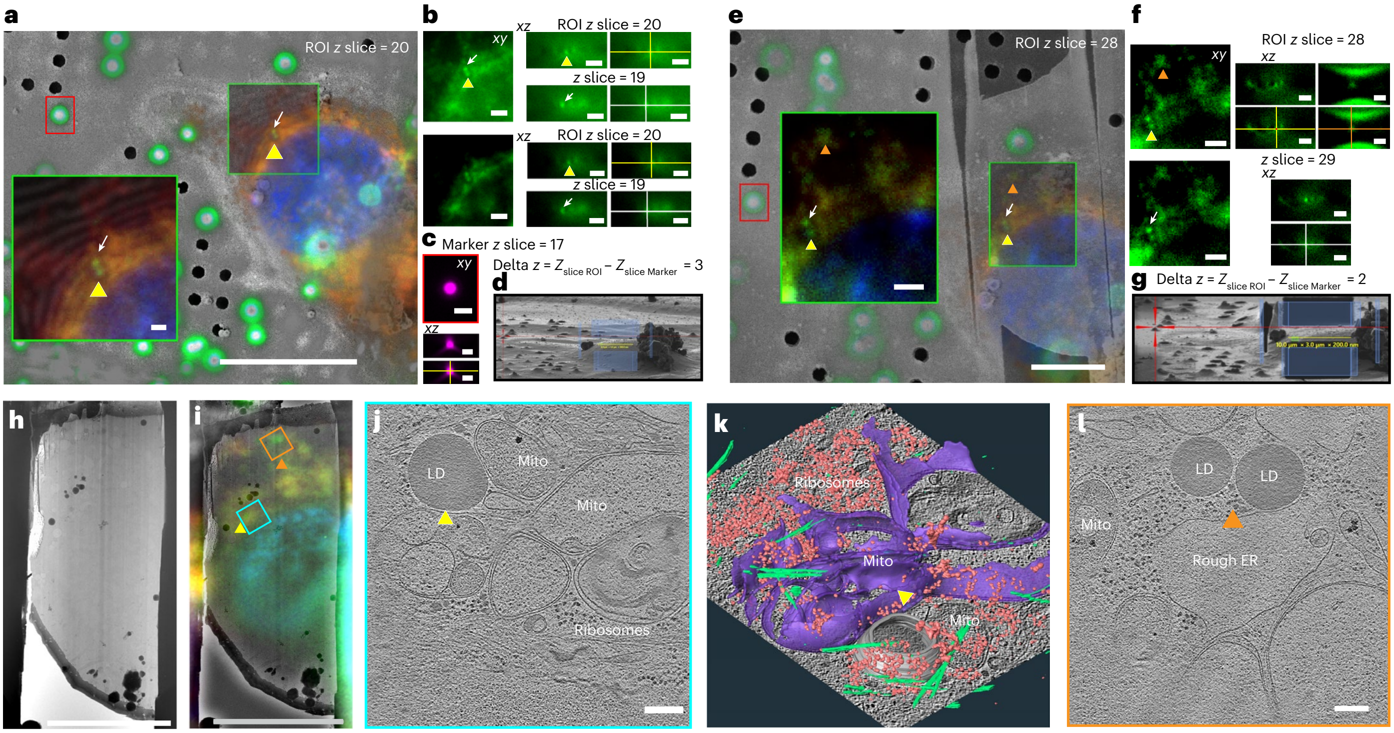

Fig. 9 | Adaptability of the iFLM-guided FIB milling-cryo-ET workflow. **a**,**b**, While two adjacent LDs (yellow arrowhead and white arrow) were the initial ROIs (**a**), the iFLM *z*-stack along with the zoomed-in view (green boxed) revealed that the LD pair was on two *z*-planes (*z*-slices of 19 and 20 in the unmilled iFLM *z* stack), in both raw (**b**, top) and deconvoluted data (**b**, bottom) of the orthogonal *xz* views. The *z*-height difference between the LDs was ~350 nm; thus, one of them was chosen as the final ROI (yellow arrowheads in **a**–**f** and **h**–**k**) to be retained in the final 200 nm lamella. **c**, The single-pair ROI–marker (*z*-slice of marker = 17) was performed on the chosen ROI (yellow arrowhead). **d**, Owing to the positioning of the ROI close to the edge of the cell, the final milling box was adjusted to be off the center but still covers the ROI. **e**,**f**, The LD pair (yellow arrowhead and white arrow) was retained in the 3-µm-thick lamella chunk after the rough milling step, as shown in the FLM-SEM overlay of the post-rough lamella chunk (**e**) and merged iFLM fluorescent view alone (**e**, enlarged green box), and the same relative *z*-plane difference between the two LDs (*z*-slice of 28 and 29 in the lamella chunk deconvoluted iFLM *z* stack, **f**) was observed. An additional LD site (orange arrowhead in **e** and **f**) on the same *z*-plane as the ROI (yellow arrowhead in **e** and **f**) became evident. **g**, Magnified view of milled ROI as noted in **d** to display the milled regions and original placement of the final milling box. **h**–**l**, The milling process proceeded to generate the final 200 nm lamella, preserving the targeted ROI (yellow arrowhead) and an additional LD site (orange arrowhead), as shown in the TEM alone (**h**) and overlay of TEM and final iFLM (**i**) of the 200 nm lamella. Regular corelative cryo-ET was acquired at both LD sites (original LD pointed out by yellow arrowhead in **i** and **j** with the cyan boxed acquisition area, and a third LD highlighted by orange arrowhead in **i** and **l** with the orange boxed acquisition area). The segmentation analysis was performed on the ROI (yellow arrowhead) to reveal the mitochondria–LD contact (**k**). MVB, multivesicular bodies; ER, endoplasmic reticulum; Mito, mitochondria; LD, lipid droplets. Scale bars, 20 µm in **a**; 10 µm in **e**,**h**,**i**; 2 µm in **b**,**c**,**f** and insets of **a**,**e**; 200 nm in **j** and **l**.

goal. MPACT implements moderate spiral pattern shifts to spread the dose accumulated in the overlap tiles. Single-tilt series acquisition may also work better when lamellae are too small to fit in a pattern or when ROIs are near the edge of a lamella or grid bar (Fig. 9).

When setting up MPACT collections, one should consider the following[26]: (1) pattern size, (2) beam/illumination size (assuming most instruments have circular C2 apertures), (3) tile overlaps and (4) the spiral translation shift to distribute dose (reducing 'hotspots') while preserving the ROI. We commonly adopt 2 × 2, 3 × 3, 4 × 4, 3 × 4 or 3 × 5 montage patterns at pixel sizes of 3–4 Å. A larger beam size helps reduce Fresnel fringe effects but increases the number of pre-exposed areas within the montage array. In practice, we have found that Fresnel fringes affect 3.5–4% (non-fringe-free system) or 1–2% (fringe-free system) of the outer edge of a camera frame. Reducing overlap regions helps spread uneven accumulation of dose between tiles; however, careful adjustments are needed to prevent blank or black corners in stitching due to insufficient coverage. For common rectangular cameras, such as Gatan K3 (5,760 × 4,092 pixels), optimal tile overlaps are typically ~10–12% in *x* (long axis) and ~7–10% in *y* (short axis) to ensure smooth automated blending from −60° to 60° tilts. Square cameras such as Falcon 3 or 4 (4,096 × 4,096 pixels) could achieve effective blending with smaller overlaps of 10% in both axes.

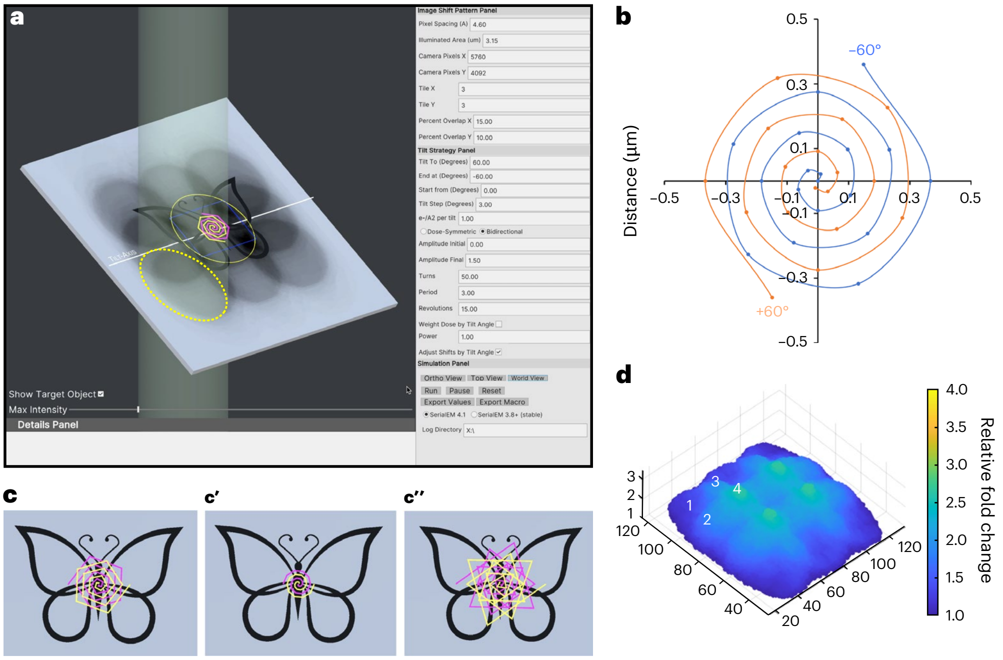

Image Shift Pattern Panel
Pixel Spacing (A) 4.60
Illuminated Area (um) 3.15
Camera Pixels X 5760
Camera Pixels Y 4092
Tile X 3
Tile Y 3
Percent Overlap X 15.00
Percent Overlap Y 10.00

Tilt Strategy Panel
Tilt To (Degrees) 60.00
End at (Degrees) -60.00
Start from (Degrees) 0.00
Tilt Step (Degrees) 3.00
e-/A2 per tilt 1.00
○ Dose-Symmetric ● Bidirectional
Amplitude Initial 0.00
Amplitude Final 1.50
Turns 50.00
Period 3.00
Revolutions 15.00
Weight Dose by Tilt Angle ☐
Power 1.00
Adjust Shifts by Tilt Angle ☑

Simulation Panel
● SerialEM 4.1 ○ SerialEM 3.8+ (stable)
Log Directory X:\

Show Target Object ☑

Fig. 10 | TomoGrapher GUI to enable optimizations of MPACT acquisition schemes via 3D simulation. **a**–**c**, TomoGrapher is an electron tomography simulation software tool to allow the user to visualize 3D tilt series acquisitions and design tilt strategies for MPACT (**a**), including different translational trajectories to spread the electron dose (default Archimedean spiral in **b** and adapted patterns in **c**, and various additional trajectories (**c′**–**c″**) upon changing the parameters in the 'Tilt Strategy Panel'). TomoGrapher utilizes a conventional right-handed coordinate system, with the stage canvas serving as the *xy*-plane, beam projection aligned along the *z* direction and the tilt axis oriented along the *x* direction. Acquisition parameters such as pixel size, camera dimension and illuminated areas are tunable by the user. The user can observe the behavior of beam elongation and pattern stretching as the stage is tilted during simulated data collection. The center of the montage tile pattern follows the spiral trajectory (yellow (**c′**–**c″**)/blue (**b**) for negative-tilting angles, pink (**c′**–**c″**)/orange (**b**) for positive-tilting angles). **d**, Two files can be exported from TomoGrapher after the acquisition scheme has been optimized: a SerialEM macro with parameters that can be directly used to run in SerialEM (3.8 and above) on a TEM, and a text file with information about electron dose accumulation per voxel, easily visualized in MATLAB (pictured in **d**) or other programs. A tutorial on how to use TomoGrapher can be found at https://github.com/wright-cemrc-projects/cryoet-montage/tree/main/TomoGrapher.

All montage schemes introduce uneven illumination over the entire tilt series[26,49]. Tile overlaps can be adjusted, but the beam-to-sample illumination becomes elongated along the axis perpendicular to the tilt axis, causing the illumination to bleed into adjacent or neighboring tile tilt series. MPACT and other schemes[26,49] include translational and/or rotational shifts of the montage pattern to spread the dose throughout the tilt series acquisition. As a result, overlap zones are reduced because the beam does not repeatedly irradiate the same area at each tilt increment. We developed TomoGrapher[26] (Fig. 10), a user-friendly cryo-ET data collection simulation tool, to visualize ROI placement and quantitatively determine dose accumulation per pixel. Using TomoGrapher, we determined that a moderate translational movement of the tile pattern along an Archimedean spiral can reduce excessive exposure present in overdosed zones of motion-free montage acquisitions by 1.5–2-fold and preserve the ROI over the entire tilt series. This and other pattern trajectories can be tested using the TomoGrapher simulator and the best collection schemes can be exported as a SerialEM Macro with optimized parameters for subsequent direct application as 'Primary Action' in the 'Navigator Acquire At Item' function. Using SerialEM 4.1, many collection parameters can be further refined and saved, including overlaps between adjacent tiles in 'Montage Setup' and 'MultipleRecord' dialogs, defocus parameters and positions for each MPACT site and related dose accumulation information in the meta data .mdoc file for downstream dose weighting filtering processes[69] (Fig. 11).

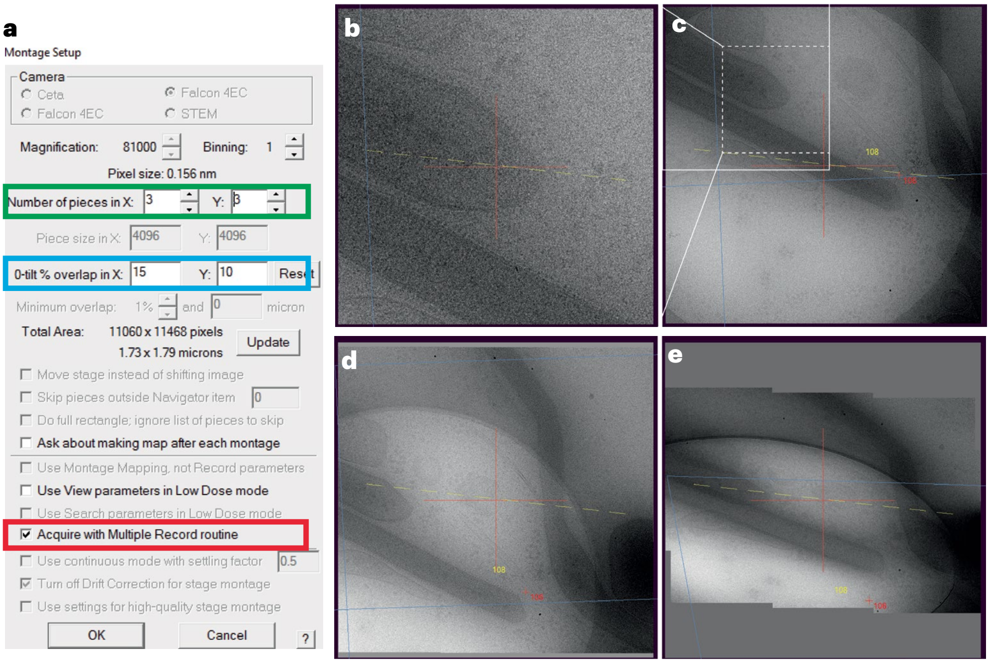

Montage Setup

Camera
○ Ceta
● Falcon 4EC
○ Falcon 4EC
○ STEM

Magnification: 81000
Binning: 1
Pixel size: 0.156 nm
Number of pieces in X: 3 Y: 3
Piece size in X: 4096 Y: 4096
0-tilt % overlap in X: 15 Y: 10
Minimum overlap: 1% and 0 micron
Total Area: 11060 x 11468 pixels
1.73 x 1.79 microns

☐ Move stage instead of shifting image
☐ Skip pieces outside Navigator item 0
☐ Do full rectangle; ignore list of pieces to skip
☐ Ask about making map after each montage
☐ Use Montage Mapping, not Record parameters
☐ Use View parameters in Low Dose mode
☐ Use Search parameters in Low Dose mode
☑ Acquire with Multiple Record routine
☐ Use continuous mode with settling factor 0.5
☑ Turn off Drift Correction for stage montage
☐ Use settings for high-quality stage montage

Fig. 11 | MPACT acquisition in SerialEM 4.1. Screenshots associated with running an MPACT tilt series collection in SerialEM 4.1 on a square camera (Falcon 4i, 4,096 × 4,096) and Titan Krios G4. **a**, The standard Montage setup window: the tile pieces (or size) of the cryo-ET montage (green box) and the image shift that defines the beam-image shift for each tile and their overlaps (blue box) can be directly edited by turning on the Multiple Record option (red box). **b**–**e**, A well-stitched live overview of a 2 × 2 montage is displayed at the end of each collection per tilt in the SerialEM main canvas window, from 0° (**b** and **c**), 21° (**d**) and 60° (**e**), where **b** is the zoomed-in view of the dashed white box in **c**, of the first subtile (solid white box in **c**). The center of the FOV (red cross) and tilt axis (yellow line) are indicated in the SerialEM main canvas view.

Image processing: montage tile stitching and individual tile tilt series generation, segmentation, coordinate-based particle extraction and alignment for STA

MotionCor2 is used for alignment and correction of raw movie frames/fractions from the MPACT data[70]. For montage tilt series, the tile frames per tilt can be registered and stitched together using designated beam-image shifts and linear cross-correlation. We find that this approach routinely provides robust and seamless blending without user intervention up to ±60° tilts. Stitched montage tilt series or individual tile tilt series can then be reconstructed using IMOD[34]. After processing, one $m \times n$ (for example, 3×3) MPACT acquisition renders $m \times n + 1$ tomograms (for example, $3 \times 3 = 9$ individual tile tomograms + 1 montage tomogram). To reduce computational overhead, we routinely extract particles from tile tomograms for higher-resolution STA structure determination. This STA processing workflow includes PEET[41], Dynamo[40] and Relion[42]. Data may be processed using other programs such as EMAN2 (ref. 71) and M-Relion-Warp pipelines[72]. Tomographic segmentations can be generated with Amira Software[36] (Thermo Fisher Scientific), EMAN2[37], Dragonfly[38] or other popular software packages. We use Amira Software and other programs[38,73] for quantitative analysis of the resulting tomograms.

Materials

Biological samples

In this protocol, we demonstrate the workflow using HeLa cells (American Type Culture Collection (ATCC) CCL-2) that were fluorescently labeled with mitochondrial, nuclear and LD-specific dyes. We show advanced workflows used to produce well-vitrified grids of patientderived EOS cells. In addition, we have used this approach with A549 cells (ATCC, CCL-185), BEAS-2B cells (ATCC, CRL-9609) and primary *D. melanogaster* third-instar larval neurons (the strain elaV-Gal4, UAS-CD8::GFP maintained and kindly provided by the Wildonger laboratory, University of California).

Reagents

- MilliQ water
- Dulbecco's PBS, Ca^{2+} and Mg^{2+} free (DPBS; Lonza, cat. no. 17-512F)
- DMEM, 4.5 g/L glucose (Lonza, cat. no. 12-604F)
- Fetal bovine serum (HyClone, cat. no. SH30071)
- Penicillin–streptomycin–amphotercin B antibiotic-antimycotic solution, 100× (Corning, cat. no. 30-004-CI)
- Ethanol (190 proof, 95%, Decon Labs)
- Water for cell culture applications (Lonza, cat. no. 17-724F)
- Trypsin/EDTA (Sigma-Aldrich, cat. no. T4049)
- Trypan blue (Gibco, cat. no. 15250061)
- Collagen I, Bovine (Gibco, cat. no. A1064401) or Collagen I, rat tail (Gibco, cat. no. A1048301)
- Glycerol (≥99%) (Fisher Chemical, cat. no. 56-81-5)
- MitoTracker Dyes (ex/em 581/644, Thermo Fisher Scientific cat. no. M22425)
- Hoechst-33342 live-cell nuclear acid stain (ex 361 nm, Thermo Fisher Scientific cat. no. 62249)
- BODIPY (excitation/emission (ex/em) 493/503, Thermo Fisher Scientific cat. no. D3922)
- CellBrite Steady Red cytoplasmic membrane dye (ex/em 562/579 nm, Biotium, cat. no. 30107-T)
- FluoSphere, 1 µm, red fluorescent (ex/em 580/605 nm, Thermo Fisher Scientific cat. no. F13083)
- TetraSpeck, 0.2 µm fluorescent (ex/em (color) 360/430 nm (blue), 505/515 nm (green), 560/580 nm (orange) and 660/680 nm (dark red), Thermo Fisher Scientific cat. no. T7280)
- FluoSphere, 40 nm, dark red fluorescent (ex/em 660/680 nm), Thermo Fisher Scientific, cat. no. F8789)
- Industrial-grade liquid nitrogen (22 psi, Airgas, cat. no. NI 230LT22)
- Dry research-grade ethane gas (99.999% purity, Airgas, cat. No. ET R35)
- Dry ultrahigh purity (UHP) nitrogen gas (Airgas, cat. no. NI UHP230LT350, or cat. no. NI UHP300)
- Dry UHP argon gas (Airgas, cat. no. AR UHP300)

  ▲ **CAUTION** Handling liquid nitrogen (LN_2) should be done in a fume hood with a venting snorkel or in a well-ventilated area, wearing appropriate personal protective equipment (PPE), including gloves, goggles, a laboratory coat and closed-toe shoes.

  ▲ **CAUTION** Ethane is a flammable gas and a fire hazard. Do not use it near an open flame. Handling ethane and/or liquid nitrogen should be done in a fume hood with a venting snorkel, in a well-ventilated area, or with proper PPE, including gloves, goggles, a laboratory coat and closed-toe shoes.

General equipment/consumables

- CO_2 incubator for mammalian cell culture (for example, BINDER C170, BINDER GmbH)
- Biological safety cabinet
- Chemical hood or snorkel (for the freezing container (ethane and LN_2 cups) and Aquilos sample shuttle)
- Inverted light microscope for live-cell imaging (DMi8, Leica Microsystems)
- C-Chip hemocytometer for cell counting (Incyto, cat. no. MCT-150-C)
- Glass-bottom cell culture dishes (MatTek, cat. no. P35G-0-20-C)
- Pipette and pipette tips

Specific equipment/consumables

- Aquilos 2 Cryo-FIB equipped with an integrated fluorescence microscope (iFLM) system (Thermo Fisher Scientific), or Aquilos 1 or 2 or other dual-beam microscope system

equipped with an integrated fluorescence objective, for example, METEOR system (Delmic) and a cryo-stage
- GIS with organoplatinum (trimethyl [(1,2,3,4,5-EDTA)-1 methyl-2, 4-cyclopentadien-1-YL] platinum) (in chamber, Aquilos, Thermo Fisher Scientific)
- Sputtering system with platinum target (in chamber, Aquilos, Thermo Fisher Scientific)
- Sample transfer system including transfer station (for clipped grid loading onto the AutoGrid shuttle under LN_2), transfer rod (to transfer the shuttle from transfer station to the microscope), vacuum pump (to pump or vent the transfer rod to proper states) and screwdriver (to close or open the shuttle clamp) (Thermo Fisher Scientific)
- Clipping station and clipping tools (Thermo Fisher Scientific, cat. no. 1000068)
- Cryo-FIB AutoGrid and C-clip ring (Thermo Fisher Scientific, cat. no. 1205101, 1036173)
- AutoGrid Tweezers (Ted Pella, cat. no. 47000-600)
- (optional) Long operation kit (Dewar and heat exchanger modifications) Gen 1 (SubAngstrom)
- Leica ACE 600 (Glow discharge, Leica Microsystems)
- Cryo-transmission electron microscope with AutoGrid loading capacity, for example, Titan Krios 300 kV TEM (Thermo Fisher Scientific).
- Leica EMGP plunge freezing machine (Leica Microsystems)
- Filter paper, for example, Whatman grade 1 (Whatman, cat. no. 1001-325)

Software

- iFLM Software v1.4.0 and above (Thermo Fisher Scientific)
- MAPS Software v3.20 and above (Thermo Fisher Scientific)
- AutoTEM Software v2.4.0 and above (Thermo Fisher Scientific)
- xT Software user interface and server v32.1.1 (Thermo Fisher Scientific)
- SerialEM v3.8 and above (https://bio3d.colorado.edu/SerialEM/download.html)
- CorRelator v1.3.0, 1.40.0, and above (https://github.com/wright-cemrc-projects/corr/releases)
- MPACT acquisition (https://github.com/wright-cemrc-projects/cryoet-montage/tree/main/SerialEM) and preprocessing including motion correction and tilt series stitching and tile sorting (for SerialEM v3.8 and v4.0: https://github.com/wright-cemrc-projects/cryoet-montage/tree/main/Python; for SerialEM v4. 1 and above: https://github.com/wright-cemrc-projects/cryoet-montage/tree/main/Bashscripts)
- TomoGrapher (https://github.com/wright-cemrc-projects/cryoet-montage/tree/main/TomoGrapher)
- (Optional) Leica LASX CORAL microscope software v. 4.6.2.28352 (Leica MicroSystems)
- MotionCor2 (UCSF)
- IMOD 4.11 and above (https://bio3d.colorado.edu/imod/)
- MATLAB R2020 and above (MathWorks)
- Amira 3D Software 2023.2 and above (Thermo Fisher Scientific)
- Computational toolbox for ultrastructural quantitative analysis of filament networks in cryo-ET (https://schurlab.ist.ac.at/downloads/)
- Fiji (macOS x86-64, https://imagej.net/software/fiji/downloads) and DeconvolutionLab2 (Richardson-Lucy algorithm, https://bigwww.epfl.ch/deconvolution/deconvolutionlab2/)

Reagent setup

- Cell culture media, for example, complete DMEM containing 10% vol/vol HyClone FBS and 1% vol/vol penicillin–streptomycin (Thermo Fisher Scientific) for HeLa cells
- 10% vol/vol glycerol (10% glycerol in cell culture grade water)
- 70% vol/vol ethanol (70% of 190 proof ethanol in MilliQ water)

Equipment setup

System preparation: to minimize potential ice buildup and clogging of the N_2 gas lines that cool the Aquilos 2-stage and shield the FIB-SEM chamber, we recommend flowing room-temperature N_2 gas continuously for one hour at a full flow rate of 190 mg/s through the system. After this period, the system and stage can be cooled by inserting the heat exchanger into the large LN_2 dewar, as described previously[43]. The N_2 gas source should be UHP (>99.999 % purity), obtained from either a high-pressure compressed gas cylinder (Airgas) or 350 PSI liquid dewar (Airgas).

Procedure

Preparing EM grids

● **TIMING 1–2 d**

1. Prepare 4–8 Au Quantifoil SiO_2 or carbon grids (200 mesh) by first coating them with an extra layer of carbon (1–2 nm for SiO_2 foil and 5 nm for carbon foil) via evaporation (ACE600, Leica Microsystems), followed by glow discharge with air to ensure adequate hydrophilicity under vacuum (0.1 Torr), 10 mA for 60 s (ACE600, Leica Microsystems). Ultimately, the foil surface will be slightly negatively charged. The extra coating of carbon is optional, but is often used for improved grid stability that tends to result in better cell attachment.
2. In a sterile environment such as a biosafety cabinet, clean the glow-discharged Au grids as described previously[6] to ensure consistent cell adherence. Briefly, the grids are transferred to the central glass region of a MatTek dish containing 70% ethanol for 15–20 min, followed by three rounds of water wash (cell culture grade) and one round of DPBS (2 ml per wash). Optionally, coating with an extracellular matrix protein, for example, collagen, fibrinogen or poly-L-Lysine is recommended in place of an overnight soak in complete medium (Fig. 6d,e). The coating parameters of the extracellular matrix protein may need optimization, including duration, concentration and temperature. For HeLa cells, coating grids with collagen includes an incubation of 30 min at 37 °C in a CO_2 incubator; and for EOS cells, fibronectin is used for coating with 2 h of grid incubation at 37 °C in a CO_2 incubator (Fig. 6d,e).
3. (Optional) For cultured cells to be FIB milled, they will need to be in FIB-accessible positions, which is the central area of the grid (~5 squares (200 mesh) away from the grid center) and at each grid square center. To further direct cell deposition and growth, we use the Alvéole PRIMO[31,61] micropatterning process to tailor the grid surface. A detailed step-by-step procedure can be found in our previous work[31].
4. Once the grids are ready, detach adherent cells from culture flasks by digestion (0.25% trypsin for 3–5 min at 37 °C with 5% CO_2) and seed the cells at the density of $0.25–0.35 \times 10^5$ cells per MatTek dish that contains 2–3 grids. Cell seeding density is a critical factor for achieving adequate target labeling and cell vitrification via plunge freezing. The optimal cell density depends on cell type, overall cell dimensions, their tendency to spread and special cell treatments (if used). In practice, we find that one cell per square generally renders good ice vitrification for eukaryotic cells ($0.5–0.75 \times 10^5$ total cells per MatTek dish) with a thickness up to 15 µm. These cells, for example, HeLa, A549, BEAS-2B and activated EOS cells (Fig. 6b,d,e), maintain morphologies consistent with those from live-cell imaging experiments. When vitrifying samples by plunge freezing, cells on the grid should not be allowed to reach 100% confluency.
5. Place the MatTek dish in the incubator at 37 °C with 5% CO_2 and monitor cell growth using a light microscope (4–6 h increments) to identify suitable cell confluency. Typically, we aim for 30–50% confluency with well-attached and spreading cells before live-cell labeling or subsequent manipulations. To maintain sterile conditions and comply with institutional biosafety regulations, EM grid preparation steps with cells, viruses and other materials should be performed in BSL-approved rooms and in a biosafety cabinet. Depending on the biosafety level, corresponding required safety measures are needed.
6. Once cells have reached the desired level of growth, fluorescently label the cells with low cell toxicity live-cell stains and/or perform transfection, infection or transduction experiments. For experimental details associated with transfection, infection, or transduction, please refer to the step-by-step protocol in ref. 6. For infected samples, the sample may need to be inactivated via gentle chemical fixation as well.

Plunge freezing of the grid

● **TIMING ~1–1.5 h for 8 grids, including clipping and system setup.**

7. After setting up the EMGP system, including ethane condensation and chamber conditions, wash the on-the-grid cells (2–3 grids per MatTek dish) with 1× DPBS and transfer one grid at a time to another MatTek dish prefilled with 2 ml of 10% (vol/vol) glycerol/DPBS. Incubate the grid in 10% glycerol for 2–3 min. The EMGP chamber conditions (temperature and humidity) should be adjusted based on cell types and equilibrated before loading any grids. The goal is to minimize environmental stresses for the cells. The humidity is generally set at 95–100% to avoid liquid evaporation, premature grid drying and cell dehydration.
8. Pick up the grid using the EMGP freezing tweezers, quickly load it onto the plunging rod and follow the instructions on the EMGP touchscreen.
9. (Optional) Pipette 2 µl of a diluted FluoSphere solution onto the cell side of the grid and incubate for 2 min. If a second or third application is desired to increase the FluoSphere concentration on the grid, open the chamber door and manually blot away the 4 µl with blotting paper from the bottom or side of the grid. Quickly apply an additional 2 µl of diluted FluoSphere and allow for another 2-min incubation before advancing to the 'Blot' step on the touchscreen.

   ▲ **CRITICAL** The use of FluoSpheres less than 1 µm as extracellular markers is not recommended because the smaller size limits their differentiation from ice chunks and other possible contaminants. Optimization of the FluoSpheres, including concentration, emission wavelength selection and sphere size, is necessary. In our case, the stock FluoSphere solution is diluted with cell culture-grade water or PBS to achieve ~10 beads per grid square (1:800 to 1:1,000 vol/vol). Then, it is sonicated at 35 kHz in the water bath for 10 min to prevent aggregation on the grid during the freezing process.
10. Proceed to the procedure of 'Blot' in the touchscreen and transfer the frozen grid to an empty slot in the grid box. Repeat Steps 7–10 to freeze more grids. Typically, with our EMGP, blot times of 14–18 s are used for grids with 30–50% cell confluency.

    ◆ **TROUBLESHOOTING**

    ■ **PAUSE POINT** The frozen sample can be stored in a liquid N_2-filled storage dewar until needed for FIB milling, cryo-FLM and cryo-TEM imaging.
11. Frozen grids will need to be clipped before loading into an Aquilos cryo-FIB-SEM system. To orient the sample correctly in the cryo-FIB shuttle for FIB-milling as well as the autoloader cassette for cryo-TEM imaging, we make fiducial marks on the AutoGrid using a Sharpie marker. For step-by-step clipping procedures, please refer to previous work[43].

    ▲ **CRITICAL** For cryo-FIB milling, it is recommended to use an AutoGrid clip ring with a square indentation on the edge[43]. This allows for a shallow milling incident angle to maximize the accessibility of the ion beam to the sample (cells) on the grid, as well as to optimize lamella size and throughput. Note that standard metal clip rings can be used for FIB milling, provided a higher milling angle is considered. There are marks etched on AutoGrids; however, it can be challenging to see them for aligning and orienting the grid under liquid N_2. We use a Sharpie to mark opposite the milling slot to prevent potential ink deposition on the lamella surface during milling. More details can be found online (Chapter 4: data collection on https://cryoem101.org/chapter-4-et/).
12. (Optional) Frozen grids can be loaded onto a cryo-FLM system and imaged at LN_2 temperature. We use a THUNDER cryo-CLEM (Leica) system for wide-field imaging and a Stellaris cryo-CLEM (Leica) system for confocal imaging. To minimize ice contamination that accumulates over time when using a cryo-stage, we recommend screening and collecting grid overviews using wide-field imaging and acquiring only cryo-confocal stacks at specific ROIs. Please refer to the previous work[6] for detailed steps and instructions on cryo-CLEM imaging.

Cryo-FIB-SEM system setup and sample loading

● **TIMING ~3 h based on the instrument**

Detailed procedures for microscope cooling and sample loading have been published previously[43] (Steps 25–50). This original protocol outlines the steps using the Aquilos 1 system. In this current protocol, we focus on the Aquilos 2 and 2 + iFLM systems (cryo-iFLM-FIB-SEM).

13. Open the N_2 gas flow to flush the cooling lines of the Aquilos 2 cryo-iFLM-FIB-SEM system at the rate of 190 mg/s in FlowView for 1 h to avoid the formation of small ice crystals and the potential interruption of the cryo-cooled N_2 gas flow during the operation.
14. Slowly insert and secure the heat exchanger into the LN_2 dewar, maintaining a gas flow rate of 190 mg/s. The flow rate may be machine-dependent. Increasing the flow (for example, 215 mg/s) may be needed for some systems.
15. Once the temperature of both shield and stage reaches ~−194 °C, maintain the gas flow at 190 mg/s or higher, and wait for ~30 min for temperature stabilization before sample loading. Ensure the vacuum pressure has reached the 10^{-7} mbar range (~10-fold less compared with the room temperature vacuum pressure value) when the temperature (shield/stage) has stabilized at ~−194 °C.

3D correlative cryo-FIB milling with integrated FLM

● TIMING 1.5–2 h per lamella site, including iFLM imaging, rough milling, and final polishing in AutoTEM, with ~10 min of grid overview SEM imaging and 1–2 min of GIS coating

16. Acquire a tile set of the loaded grid(s) in MAPS (3.21 and above) following the previously published procedure[43] (Steps 51–59), using low voltage (2 kV) low current (25 or 50 pA) SEM imaging state (standard mode, Everhart–Thornley detector).
17. (Optional) Import the external FLM or cryo-FLM grid montage or site-specific image stacks or 2D images (JPEG, TIF, PNG, MRC format) into MAPS by right-clicking on the 'layer' object on the left panel of the MAPS interface (Fig. 12). The software will allow the user to select 'import image' function. Alternatively, it is possible to import the files (.xlef), with the associated metadata, from LASX imaging software suite used on a Leica Stellaris cryo-confocal system into MAPS. The XLEF file indicates the file paths for actual images (.tif), which should also be accessible by the Aquilos microscope PC. Note, compatibility is dependent on the software versions. We find that importing images has worked well on all the MAPS v3.27 and above and current LASX versions (Leica Coral v. 4.6.2.28352 and above). Alignment between FLM and SEM is still required (Step 18) for the case of '.xlef' imports.
18. (Optional) Align the external FLM or cryo-FLM grid montage or overview with the high-resolution SEM tile set montage by right-clicking on the imported images, selecting 'Align' from the menu and following the pop-up instructions in MAPS to perform the alignment (Fig. 12a,c). If fluorescent ROI are not present in every cell identifiable by SEM, it is helpful to have a RT-FLM or cryo-FLM grid overviews to direct where iFLM imaging may need to be performed.
19. Scan and search over the high-resolution SEM tile set or the FLM-SEM overlay to identify lamellae sites for iFLM imaging. The millable and TEM-accessible sites should be within a radius of ~600 µm from the grid center. Once a site is found, right-click on the SEM tile set and select 'Add a lamella site' function. Milling sites can be chosen on both Grid 1 and Grid 2 SEM tile sets simultaneously if two grids are loaded.
20. Go to the Mapping position of a region where one or multiple lamella sites are present by highlighting one 'Lamella' and clicking 'Drive To next to Mapping Position' in MAPS (Fig. 12a, purple box, bottom area).
21. Open iFLM software and click the 'SEM to LM' tab on the top Stage and Objective Control panel (Fig. 13a). The shuttle will move to the designated LM stage position. It is essential to go to the Mapping position of the region (or ROI) before iFLM imaging to avoid having a stage touch or crash when the shuttle moves from the SEM position to the LM position. Do not directly type the iFLM imaging position in the xT GUI, because the shuttle is required to move in a specified sequence order to avoid encountering the LM objective. Always use the SEM to LM tab in the iFLM software GUI.
22. Find the LM focal plane by inserting the objective and turning on the 'Live View' function with 'Auto Contrast' checked. Change the step size (µm) to 1,000 when the 'Absolute Piezo Position (µm)' is at ~0. Select 'Reflection' mode and setup the acquisition settings as presented in Table 3. Find the focal plane of the ROI or foil by manually moving the objective ('Retract' or 'Advance'). Use larger step sizes to Retract or Advance to focus, and gradually

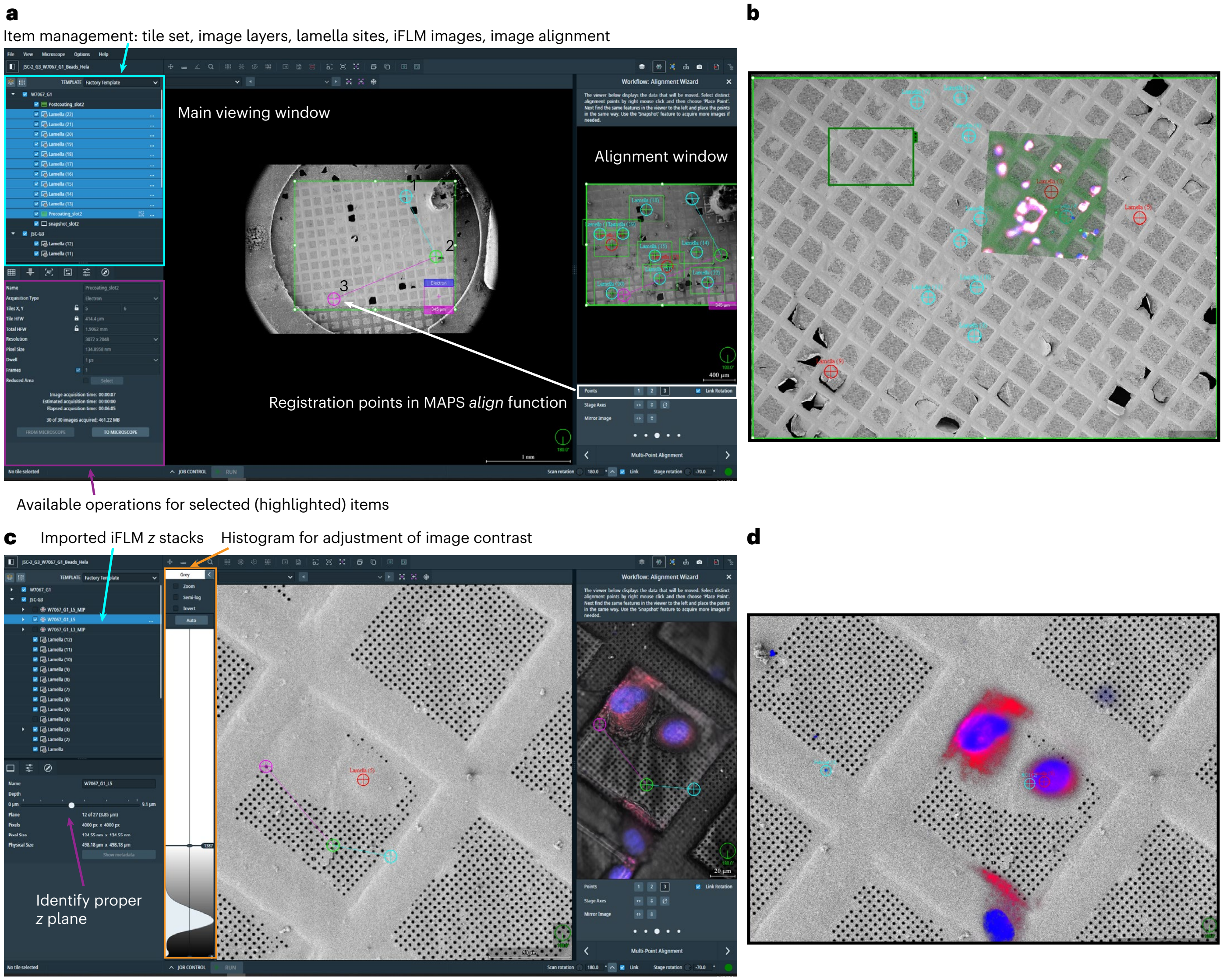

Fig. 12 | MAPS software for tile set collection and FLM image alignment. Screenshots of the alignment procedure, initial importation of an iFLM image *z* stack and fine-tuned iFLM-SEM overlay in MAPS. **a**, The alignment between the initial and postsputtering GIS tile sets. The Main viewing window (left) displays the grid tile set post sputtering and GIS coating while the Alignment window (right) displays the grid tile set before any coating procedure with lamella sites highlighted in blue in the Item Management bar. **b**, MAPS display of imported initial iFLM image stacks via a .tfs file with the appropriate stage transformation and correlation, before any alignment adjustment. **c**, Alignment between the postsputtering/GIS tile set. **d**, An imported iFLM image stack and final display of fine-tuned FLM-SEM overlay after further alignment adjustment in **c**.

decrease the step sizes as the objective approaches the grid surface. We usually start with a step size of 1,000 until we observe very rough shapes and features in the live view, and then change to 100 or 50 when a grid square begins to appear. We then use 10 or 2.5 to find the mesh and carbon film, and finally use 1 or 0.25 to fine-tune the focal plane.

23. Stop the live view when the targeted cell is in focus and switch to a fluorescence channel (385 nm, 470 nm, 560 nm or 625 nm) in ‘Fluorescence’ mode. Refer to Table 3 for the FLM imaging setup.
◆ **TROUBLESHOOTING**
24. Use a fine ‘Step Size’ of 1 or 0.25 µm to find the focal plane of the ROI under live view in ‘Fluorescence’ mode and set up the iFLM *z*-stack ‘Start’ and ‘End Positions’ in the ‘Stack Acquisition Settings’ in the iFLM GUI. Set the slice distance to 0.35 µm. Select a file name

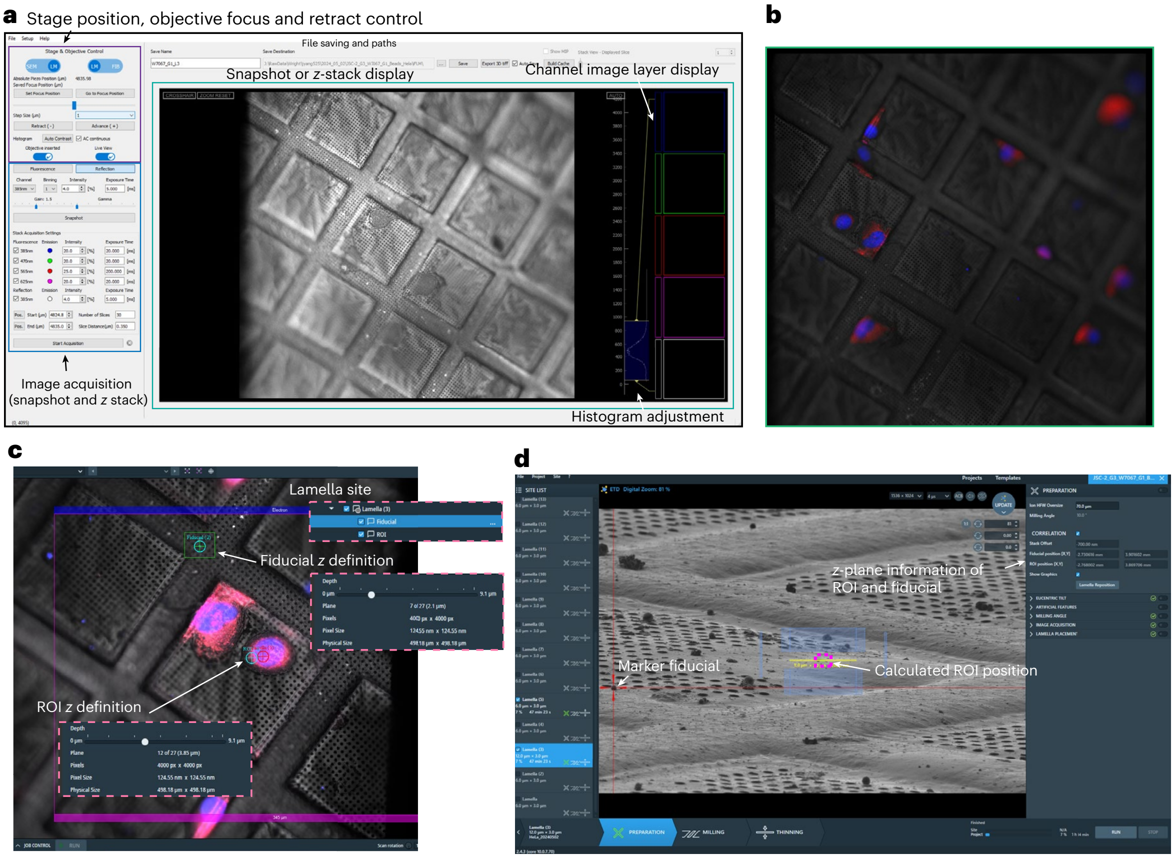

Depth
0 µm 9.1 µm
Plane 7 of 27 (2.1 µm)
Pixels 4000 px x 4000 px
Pixel Size 124.55 nm x 124.55 nm
Physical Size 498.18 µm x 498.18 µm

Depth
0 µm 9.1 µm
Plane 12 of 27 (3.85 µm)
Pixels 4000 px x 4000 px
Pixel Size 124.55 nm x 124.55 nm
Physical Size 498.18 µm x 498.18 µm

Fig. 13 | Main software packages (iFLM, MAPS and AutoTEM) for the streamlined single-pair ROI–marker FLM-guided automated FIB milling. **a**–**d**, Screenshots of the three main software program GUIs (iFLM software GUI (**a** and **b**), MAPS 3.27 GUI (**c**) and AutoTEM 2.4 GUI (**d**)) for the workflow: Step 1 in iFLM software v1.3.0 GUI (**a**) and display with acquisition channels on **b**, where the stage is controlled to move between FLM, SEM and FIB positions and cryo-FLM stacks are acquired and saved; Step 2 in MAPS software v3.27 (**c**), where the cryo-FLM image stacks acquired from iFLM software (**a**) are imported and single pair ROI–marker fiducial *xyz* positions are defined; Step 3 in AutoTEM Software 2.4 (**d**) where the defined single-pair ROI–marker position is imported from MAPS and the milling box can be automatically positioned via 'Lamella Reposition' around the calculated ROI position based on the marker fiducial value.

in the 'Save Name' field and specify the file saving path in the 'Save Destination' field. The 'Auto Save' function can be checked in the iFLM 1.3 (Fig. 13a).

▲ **CRITICAL** We recommend using a sample rate ('Slice Distance') of 0.35 µm for optimal *z*-information retrieval and a stack size of 0.35 µm for iFLM. Always collect both reflection and fluorescence mode data per site by checking the 'Reflection' in the 'Stack Acquisition Setting' section. The user can use the slider or clipping box located under 'Stack View' in the top-right corner to navigate through the slices after completing one site. The acquired iFLM raw image stacks can be processed via deconvolution externally to achieve better visualization (Fig. 4). The raw image stacks are associated with proper stage positions stored in .tfs files. See Step 29 below for more details.

◆ **TROUBLESHOOTING**

25. Go back to the SEM mapping position by clicking the LM to SEM tab under the Stage and Objective Control in iFLM (Fig. 13a).
26. Perform inorganic platinum (Pt) sputtering and organic Pt deposition via GIS by following previously published procedures[43] (Steps 76–79). The basic method involves an initial sputter coating of Pt, followed by GIS Pt deposition and an optional second sputtering of Pt to enhance sample conductivity and charge dissipation.

▲ **CRITICAL** Pt coating, particularly the organic Pt GIS deposition, is crucial for generating thin lamella with few curtaining artifacts. We recommend measuring the GIS and sputtering

Table 3 | iFLM imaging setting

	Step size (μm)	Channel	Intensity (%)	Exposure time (ms)[a]
Initial site identification	1,000, 500, 100, 10, 2.5	Reflection	2–5	2–10
ROI identification	1, 0.25	Fluorescence	<35[b]	100–800 or longer

[a] The regular iFLM system is equipped with a 12-bit digital camera. In general, we aim to capture images with final signals in the range of 200–2,000, thereby avoiding under- and oversaturation of fluorescent signals. [b] We recommend setting the intensity to a maximum of 35% of the full illumination power at the exit pupil of the NA = 0.7 objective. The maximum irradiance measured at the exit pupil varies depending on the wavelength of the illumination LEDs used. When the irradiance of each LED is set to 35% electronically, the measured irradiance values are: 1.53 W/cm^2, 0.49 W/cm^2, 0.62 W/cm^2 and 0.57 W/cm^2 for LEDs with peak wavelengths of 385 nm, 470 nm, 656 nm and 625 nm, respectively. If the ROI signal remains weak and the image is noisy, we recommend increasing the exposure time.

Pt deposition rate on a silicon wafer or a clean Quantifoil grid and adjusting the flow rate, if necessary, by changing the position of the GIS needle relative to the grid. The optimal flow rate is system dependent. Regardless, its deposition rate should be controllable within a reasonable time window. We adjust the rate to allow for 2–3 μm GIS Pt deposition in ~1 min (40–60 nm/s). We also find that the quality of the GIS Pt coating depends on the size, shape and location of the samples on the grid, enabling automated polishing in 'AutoTEM'. We shorten or extend the GIS deposition time for biological samples that vary in size and shape. The deposition angle can also be adjusted to achieve a better coating. For example, curved surfaces present challenges for uniform coating. Changing the angles that come from a shallower or milling angle could help result in better deposition and a longer GIS leading edge for protection[74]. For sputtering, we find that an initial 50–60 nm of inorganic platinum coating, before GIS, and a second round of 15 nm after GIS deposition work well to dispatch charge. Additional sputtering may be performed throughout the milling process if the grid is too icy or the sample generates excessive charging artifacts. The sputtering rate can be adjusted by varying the current and time. In practice, we use 20 mA in conjunction with a time variation.

◆ **TROUBLESHOOTING**

27. Acquire a second post-Pt coating high-resolution tile set (as in Step 16) by placing a new tile set over the grid region and start 'Run'. The 'copy grid' function can be accessed by right-clicking on the original tile set. This will generate a new unacquired tile set with the same imaging setting as the original one.
28. Select the original tile set acquired before the Pt coating in Step 16 and all lamella sites identified on this original tile set (Fig. 12a). Right-click on the original tile set and select the 'align' function. It will enter the three-point correlation steps. Follow the instructions in MAPS to finish the correlation. In the end, all lamella sites identified in the previous pre-Pt coating tile set should be transferred to the current post-Pt coating tile set montage to ensure correct site relocation in AutoTEM.
29. Import the iFLM image stacks by right-clicking on the layer where the post-Pt coating tile set is located and selecting the 'Import Image' function. Select the .tfs file associated with the corresponding iFLM image stack to import (Fig. 12b).

    ▲ **CRITICAL** The .tfs file contains the stage coordinates required for transformation between FLM and SEM mapping positions. This supports the placement of the imported iFLM image stacks at the corresponding SEM mapping positions of the sites in MAPS. However, the transformation stored in the iFLM configuration file is generally calculated using a grid that may or may not have the same geometrical topology as the sample grid. The imported iFLM image stack will be placed near the corresponding SEM mapping sites; generally, an additional alignment step is required. If the .tfs file is corrupted or missing, it is possible to import the iFLM image stacks in TIFF format. In this case, no stage-related coordinate transformation will be applied.
30. Align the imported iFLM image stack with the post-Pt coating tile set using the 'align' function by right-clicking on the iFLM image stack. Pick three points that are well distributed near or around the ROI. Go through the *z*-stacks from the iFLM in reflection or fluorescence channels to find the focal planes for the three registration points (Fig. 12c).
31. Identify the fluorescence signal of interest with the specific fluorescence channel while going through the *z*-stack in MAPS. Add the signal spot of interest as one ROI on its focal

plane by right-clicking on the imported iFLM in the MAPS main viewing display and selecting 'Add as ROI' to the associated lamella site (Figs. 12c and 13c).

32. Identify an object near the ROI as a marker on its focal plane while going through the *z*-stack in MAPS. Add this signal as a marker on its focal plane by right-clicking on the imported iFLM in the MAPS main viewing display and selecting 'Add as Marker' to the associated lamella site (Fig. 13c).

    ▲ **CRITICAL** To achieve precise targeting and minimize correlation errors, the marker needs to be unambiguously identifiable in iFLM, FIB and SEM (Figs. 1, 5, 8 and 9). A trench milled on or close to the grid bar, or even on the support foil (Fig. 6, L-shaped milling pattern), could be used because it will be visible by the iFLM reflection mode. In this case, iFLM imaging will need to be done after the L trench milling. The chromatic aberration in a functional iFLM is barely detectable between channels (less than 5 nm with 200 nm TetraSpeck beads)when the fluorescence and reflection modes are correctly aligned. If external fluorescent image stacks are used to identify the pair, we recommend using 1 µm FluoSpheres as the marker and selecting the marker that is closest to the ROI.

    ◆ **TROUBLESHOOTING**

33. Identify the 'ROI' and 'marker' pair for all remaining lamella sites by repeating Steps 31–32. Each lamella site should be accompanied by one set of 'ROI' and a 'marker'. The 'ROI' and 'marker' can be adjusted or refined at any milling point.
34. Open AutoTEM and create the MAPS-linked project to import all lamella sites. AutoTEM will automatically search for live or open MAPS projects and prompt the user to create a linked milling project. Once the link or project is established successfully, all lamella sites selected in MAPS will be imported correctly to the AutoTEM project (Fig. 13d).
35. Create and design the milling template under 'Template' in the AutoTEM GUI, and apply it to all or selected lamella sites. The parameters for each lamella site can be optimized independently.
36. Start the 'Preparation' step only in an 'automatic' or 'guided' mode in the AutoTEM procedure. Uncheck or slide the 'lamella placement' step to the off position. An AutoTEM-guided milling scheme comprises sections of 'Preparation', 'Milling' and 'Thinning'. The targeted milling occurs at the Preparation step, where the milling pattern (Fig. 13d) is placed based on the single-pair ROI–marker registration in MAPS (Fig. 13c).
37. Check the 'CORRELATION' box. A pair of red crosses (marker) and a green box (ROI) will appear. Place the red cross at the center of the marker (focal plane as in iFLM) and click 'Lamella Reposition'. The milling pattern should be placed approximately at the center of the green box (ROI). Set up the milling pattern for all remaining sites.
38. Proceed with 'Milling' in AutoTEM for all lamella sites. Rough milling and micro-expansion joints are routinely milled with a current of 0.5 or 0.3 nA. The milling currents are gradually reduced to 0.1 nA and 50 pA to obtain the 750-nm-thick lamella. Refer to Table 4 for the milling parameters.
39. (Optional) We recommend performing iFLM imaging and refining the ROI and marker in MAPS after 'rough' milling in the 'Milling' step, before 'medium' milling. Repeat Steps 20–25 to do a second round of iFLM imaging of the milled material and follow Steps 31–32 and 37 to refine the ROI and marker position. The marker can be a different fiducial. Refine the milling pattern by repeating Step 37. Resume the milling afterward.

    ◆ **TROUBLESHOOTING**

40. Proceed with 'Thinning' in AutoTEM for all lamella sites. Two rounds of 'Polishing' (Polishing 1 and 2) in the 'Thinning' section consistently produce 200-nm-thin lamella. Refer to Table 4 for the milling parameters.

    ◆ **TROUBLESHOOTING**

    ▲ **CRITICAL** We recommend testing the thinning parameters on one or two unimportant sites before applying them to the rest of the ROIs. To achieve fully automated thinning, we routinely modify 'Depth Correction' based on the thickness of the GIS Pt deposition and switch between 30 and 10 pA.

41. Go to the mapping position of a lamella site by right-clicking on the lamella site in AutoTEM and selecting 'Go to preparation position'.

Table 4 | FIB milling settings for frozen eukaryotic cells in AutoTEM 2.4

	Milling					Thinning	
	Stress relief cuts	**Rough milling**	**Medium milling**	**Fine milling**	**Finer milling**	**Polishing 1**	**Polishing 2**
Trench width (nm)	350–500[a]	–	–	–	–	–	–
Trench height (µm)	8–12[a]	–	–	–	–	–	–
Trench offset (µm)	3.5–5[a]	–	–	–	–	–	–
Depth correction (%)	80	50–200[b]	160	160	160	80–100[e]	50–100[e]
Milling current (nA)[c]	0.5	0.5	0.3	0.1	0.05	0.03	0.01
Milling pattern	Rec[d]	Rec	CCS[d]	CCS	CCS	CCS	CCS
Overtilt (°)	0	0	0	0	0	0	0
Pattern overlap (%)	–	–	400	200	200	200	200
Pattern offset (nm)	–	–	800	300	250	50	0
Front width overlap (nm)	–	–	650, 650	350, 350	50, 50	–	–
Rear width overlap (nm)	–	–	500, 500	100, 100	50, 50	–	–

[a]The width, height and offset of the stress relief cuts depend on the size of the cell and the stability of the square (if there is any crack in the square). The height needs to cover most of the cell height. The offset could be 1.75–2.5 µm away from the milling box on each side, resulting in a total offset of 3.5–5 µm. A trench that is too wide or an offset that is too close will lead to instability of the lamella during subsequent milling processes. Smaller cells with nearby cracks on the support film will benefit from smaller trench widths and narrower offsets. [b]Rough milling needs to remove the material from both the top and bottom of the lamella. Larger depth corrections lead to longer milling times. The value depends on the size of the cell and the GIS thickness. In practice, we optimize on one or two sites before setting up the batch for the rest. Tall (thick) or large cells with thicker GIS coatings may require a larger depth correction. [c]Milling currents depend on the cell size and GIS thickness. The values in Table 4 serve as good starting parameters for mammalian cells with a 3–4 µm GIS coating. If the GIS is thinner and the cell is smaller, lower the milling current for the next one in the sequence, for example, 0.5 nA to 0.3 nA for rough milling. In practice, we optimize milling conditions at one or two sites before setting up the batch for the rest. All FIB milling was carried out at an instrument voltage of 30 kV. [d]'Rec' means the use of a 'rectangular' milling pattern in which the area is constantly milled line by line to reach the final depth, allowing the user to observe the milling process live. 'CCS' is an abbreviation for 'cleaning cross section', which is a milling pattern in which the ion beam mills each point at a calculated time and depth once and then raster through each line sequentially. [e]No over tilt was used in the rough or fine milling steps in these experiments, which has been shown to achieve even milling and improve lamella flatness[77]. For lamellae shorter than 20 µm in length, we find that the front and back ends of the lamella can achieve rough uniform thickness via optimizing 'Depth Correction' combined with cleaning cross-section[78].

42. Collect the final round of iFLM image stacks of this lamella by following Steps 20–25.
    ▲ **CRITICAL** It is important to collect iFLM z-stack images of the polished thin lamella that will be used for subsequent FLM-TEM correlation for targeted tilt series data collection.
43. Repeat Steps 41–42 to collect the iFLM image stacks for all remaining thin lamellae.
44. Unload and store the grids, then warm up the iFLM-FIB-SEM microscope by following the previously published sample retrieval procedurec[43] (Steps 80–101).

Correlative MPACT acquisition

● **TIMING 1 h correlative MPACT set up in SerialEM and several hours of collection, depending on the total number of collectable sites. In general, one 3 × 3 MPACT acquisition takes ~1 h to 1 h 15 min to complete on a Titan Krios**

45. Load the sample grids onto a cryogenic TEM system following the procedure[43] published previously (steps 102–103).
    ▲ **CRITICAL** It is essential to load the milled grids in the correct orientation so that the milling direction is perpendicular to the tilt axis.
46. Open SerialEM and load a preferred setting file or use the default setting file.
47. Open a Navigator file (Nav_1.nav).
48. Collect a grid low magnification overview, where lamella sites are visible, and save it as a MAP item in the Navigator file Nav_1.nav.
49. Determine the pre-tilt angle of each lamella. The '+' and '–' direction of all lamellae on one grid is determined either by observing the change in the lamella's length at low and high tilts[74] or the GIS front-end orientation. Each lamella has a pre-tilt angle based on the FIB milling angle. It would be beneficial to verify this angle using the TEM to ensure proper pre-tilt for subsequent data processing.
    ◆ **TROUBLESHOOTING**

50. Go to each lamella site and collect a low-magnification image that captures the entire lamella. The magnification, referred to as square low magnification, may vary (usually between low magnification (LM) 1,550× and LM 2,500×, with a pixel size of 50–80 Å), depending on the size of the lamella. Save this image as a MAP item in the navigator file “Nav_1.nav”. We refer to the map as a lamella site map.
51. Go through the iFLM image stack of a final 200 nm lamella and prepare one 2D image (RGB, 8 bit or 16 bit, PNG or TIFF format) with the reflection and fluorescence channels merged, where the fluorescent ROI is visible. The overall shape of the lamella will be obvious.
52. Import the 2D iFLM image to the SerialEM navigator file ‘Nav_1.nav’ with a different ‘registration number’, such as 2.
53. Open the CorRelator GUI, which is installed on the same PC where SerialEM is installed.
54. Save the navigator file (Nav_1.nav) and import it to CorRelator via the ‘Import Navigator File’ function.
    ◆ **TROUBLESHOOTING**
55. Follow the previously published step-by-step instructions (https://github.com/wright-cemrc-projects/corr) to correlate the lamella site map and the imported 2D iFLM image/map.
56. Export a new navigator file from CorRelator (Nav_2.nav) and open it in SerialEM. Upon opening and reading the Nav_2 file in the navigator, the 2D external iFLM image is correlated with the TEM map with an updated ‘registration number’ of 1.
57. Add fluorescent ROIs into the correlated iFLM image as points in Nav_2.nav.
58. Repeat Steps 55–57 for all remaining lamella sites.
    ▲ **CRITICAL** It is possible to import all 2D iFLM images simultaneously and perform correlation for all lamella sites together in CorRelator. Assign a different registration number (non-one values) to each iFLM map. While we recommend CorRelator for correlation due to its ability to incorporate flexible registration markers and provide FLM-TEM overlays, the ‘Transform items’ feature in SerialEM could be applied instead by following the procedures described previously[6,12].
59. Set up the ‘View imaging mode’ at a medium magnification (selected-area imaging range, pixel size of 15–35 Å) in the ‘Low Dose’ panel. Perform image shift registration between the low (LM range) magnification used for lamella site map acquisition and the ‘View medium’ magnification.
60. (Optional) Collect a medium magnification montage (selected-area range) at the correct pre-tilt angle for each lamella.
61. Tilt to the pre-tilt angle of the lamella and proceed to the fluorescent ROI identified on the correlated iFLM image. Center the ROI in the ‘View’ if necessary.
    ◆ **TROUBLESHOOTING**
62. Determine the MPACT montage dimension ($m \times n$) based on the fluorescent ROI dimension(s).
    ▲ **CRITICAL** The beam-image shift limitation (up to 20 µm on a modern Titan Krios G3 or G4) is a determining factor for how large a field of view the MPACT scheme can capture. In practice, we keep the MPACT pattern size below 15 µm because the focus position (beam-image shift) per MPACT tilt series needs to be at least half of the pattern size plus the beam illumination radius. To visually inspect the MPACT pattern size and the field of view it captures, we routinely open a new montage or empty file via the New Montage Setup dialog in SerialEM, click on the center of the ROI, and use ‘Show Acquisition’ in the ‘Navigator’ window. This new montage file is essentially empty and can be overwritten to different MPACT pattern sizes.
63. Collect a View image and save it as a Map item in the ‘Nav_2.nav’.
    ▲ **CRITICAL** It is essential to make sure the View image/map is taken at the correct pre-tilt angle for each lamella. Here, the View image/map is equivalent to the Anchor or Target Map in a regular tilt series batch setup.
64. Highlight this map item and turn on ‘Acquire’ and ‘New file at item’ functions in the Navigator window.
65. Check the ‘Montage images’ as the file type once the File Properties dialog opens, and enable the Acquire with ‘Multiple Record routine’. Set x and y to the corresponding m and n pieces in the subsequent Montage Setup dialog.

66. Turn on Edit Focus and Show Acquire, then adjust the focus beam position to be half the size of the montage pattern plus the record beam radius away from the center of the MPACT pattern.
67. Repeat Steps 61–66 for the remaining ROI sites on all lamellae.
68. Load the cryoMontage_SerialEM4.1.txt from Github (https://github.com/wright-cemrc-projects/cryoet-montage) into the Script window in SerialEM 4.1 or above, or cryoMontage.txt from Github (https://github.com/wright-cemrc-projects/cryoet-montage) to SerialEM 3.8 and 4.0. Alternatively, if 'TomoGrapher' is used for the collection scheme and dose optimization (Step 71), the exported macro from 'TomoGrapher' can also be loaded.

    ▲ **CRITICAL** Make sure the correct MPACT SerialEM macro is used in the corresponding SerialEM version. For SerialEM 3.8 and 4.0, the image shift that controls the overlaps between individual tiles in Multiple Record illumination needs to be edited via the SerialEM setting file. In contrast, this function has been included in the regular Montage Setup dialog. We recommend using SerialEM 4.1 or above.
69. Update the loaded SerialEM MPACT macro with the correct file saving path by editing the 'BaseDir' in the script and save. The default parameters that control the translational shifts of the montage pattern for dose distribution work well for most cases.
70. Adjust the beam size or illuminated area for the Record imaging state setup in SerialEM Low Dose Mode and collect gain references with this beam size.

    ▲ **CRITICAL** The beam size or illuminated area relative to the camera frame determines the whole captured field of view, fringe-unimpacted or 'fringeless' area, and the pre-exposed regions. We recommend adjusting the beam size to intersect the camera frame by cutting off 8–10% (pixels) in both the long and short axis directions as a starting point for magnifications of 3.5–5 Å/pixel. The more cutoff introduced, the fewer areas are pre-exposed. Note that more overlaps between tiles are needed to ensure there are no gaps or corner zones in the final stitched views. An 8–10% cutoff works well with a 10–15% overlap between tiles.
71. Determine the dose and camera setup for the Record imaging state setup in SerialEM Low Dose Mode. TomoGrapher can be installed and run to assess the accumulated dose, optimize the dose spreading strategy '(Amplitude Final (Afinal), turns, period, revolution, Adjust Shifts by Tilt Angle (correction)' parameters in the MPACT macro).

    ▲ **CRITICAL** To ensure seamless stitching, automated preprocessing and functional tile tilt series, overlaps between adjacent tiles are required. This, inevitably, introduces uneven dose accumulation in the overlapped zone. While a spiral translational shift is applied on the MPACT pattern throughout the tilt series acquisition, dropping the total dose by 30% is highly recommended. For electron-dense features, such as LDs and/or dose-sensitive samples, we may reduce the total dose by 40–50%.
72. Update the parameters in the 'Basic Settings' section of the MPACT macro, if desired, and save.
73. Choose the MPACT macro in the 'Run script as Primary Action' and turn on 'Close column valves at end' before hitting 'GO' in the 'Acquire at Items' dialog.

MPACT tile stitching, sorting and processing

● TIMING 1 h for motion correction, automated stitching and tile sorting per MPACT tilt series (3 × 3). Several hours to days for subsequent reconstruction, segmentation, and STA

74. Run the Bash scripts (SerialEM 4.1 and above) or the Python scripts (SerialEM 3.8 and 4.0) available on Github https://github.com/wright-cemrc-projects/cryoet-montage/tree/main/Bashscripts, and follow the detailed instructions online to perform motion correction, MPACT montage stitching performed at each tilt, followed by automated assembly of the stitched tilt series and individual tile tilt series sorting.

    ▲ **CRITICAL** Montage stitching per tilt before the assembly of stitched tilt series results in smaller reconstructed areas due to increased overlaps at high tilts. Larger pattern sizes or positioning the ROI in the middle of the MPACT acquisition field can help mitigate such issues.

    ◆ **TROUBLESHOOTING**
75. Reconstruct the stitched or individual tile tilt series as a regular or non-montage dataset in 'Etomo/IMOD' via patch tracking nonfiducial alignment. It is expected that both stitched

and/or individual tile tilt series display a spiral alignment trajectory before tilt series alignment. The initial 'Coarse Alignment' in Etomo/IMOD helps to align the frames roughly.

76. (Optional) Stitch the montaged tilt series during the tomogram reconstruction step in 'Etomo/IMOD' using the montage-frame alignment workflow to minimize the effects of potential second interpolations when assembling the montage at each tilt separately.
▲ **CRITICAL** The stitching may require rounds of manual fixation, especially with thicker samples and higher tilts.
77. Perform tomogram denoising, segmentation or STA using stitched or individual tile tomograms.

Troubleshooting

Troubleshooting information can be found in Table 5.

Table 5 | Troubleshooting table

Step	Problem	Possible reason	Solution
10	Poor vitrification even after addition of cryo-protectant	(1) Insufficient blotting (2) Insufficient cryo-protectant incubation (3) Samples are too thick	(1) Increase the blot time and blot force The blot condition is machine and sample dependent. The general optimization strategy is to blot the samples at various time and screen them under TEM before milling. Sufficient blotting usually leads to well-vitrified intracellular materials yet much drier foils in some cases (2) Vary cryo-protectant concentration and incubation time (3) Try a different cryo-protectant or consider switching to high-pressure freezing if the thickness is above 20 μm
23	No FLM signal	(1) Image histogram is not properly adjusted (2) Exposure time too short or source intensity too low (3) Intrinsic weak labeling	(1) Check the image histogram (Fig. 13a) (2) Check the exposure time and light source intensity, refer to Table 3 for FLM imaging setup (3) Explore other labeling tags which are more stable under cryogenic conditions or increase the occurrence (frequency) of the event
24	The same features are not aligned in fluorescence and reflection modes	(1) Fluorescence and reflection images were taken at different times (2) Fluorescence and reflection channels are not aligned	(1) Check both 'Fluorescence' channels and 'Reflection' under 'Stack Acquisition Settings' before clicking 'Start Acquisition' (2) Microscope service is needed to check alignments between individual fluorescence channels and fluorescence and reflection channels
26	Lamella did not survive automated polishing in 'AutoTEM' or lamella is broken before reaching desired thickness of 200 nm	(1) GIS deposition was not sufficient (2) The automated polishing parameters in 'AutoTEM' need adjustment	(1) Extend the GIS deposition time by 15–30 s. For smaller cells (diameter <5 μm), slightly thicker GIS generally works better in the automated polishing step (2) Lower the polishing strength by using less current or smaller 'Depth Correction', refer to Table 4
32	The z-plane information for ROI or marker cannot be added correctly	(1) A different image layer in MAPS is activated (2) The shuttle is not in the mapping position when adding ROI or marker	(1) Select the correct image layer before add ROI and marker (Steps 37–38) (2) Check the shuttle position and move it back to the mapping position from the iFLM imaging position before adding ROI or marker
39	The 'CORRELATION' box did not take the updated value from MAPS after repositioning ROI and marker in MAPS post rough milling	(1) The CORRELATION box needs to be refreshed (2) MAPS and AutoTEM might have lost communication	(1) Uncheck and check the CORRELATION box in AutoTEM (2) Confirm the communication is lost by adding an extra lamella site in MAPS to see if the site shows up in AutoTEM. If not, close and reopen MAPS and or AutoTEM. The project progress is generally saved automatically
40	'THINNING' did not start at the correct site for milling	There was a big enough stage drift or movement that caused AutoTEM to fail to align to the previous reference image	Update the stage position and reference image in the 'PREPARATION (LAMELLA PLACEMENT)' step by sliding the function back on and click RUN
49	Uncertain about the milling angle	(1) Uncertain about the direction of the pre-tilt (+ or − angle) (2) Milling angles were not recorded	(1) The scan rotation of 180° is generally turned on in both SEM and FIB views so the cells are not upside-down. If the GIS is in the same direction (front) as the SEM view, the pre-tilt angle should be negative (−), and vice versa (2) After determining the pre-tilt direction (+ or − angle), tilt to an estimated starting point such as 10° or 12° to take an image under a selected-area range magnification (pixel size of 14–35 Å) in EFTEM mode, then tilt up and down by 1° and take an image per tilt to see at which angle the image counts are the biggest. This angle will be the pre-tilt angle

Table 5 (continued) | Troubleshooting table

Step	Problem	Possible reason	Solution
54	The images listed in the SerialEM navigator file (Nav_1.nav) cannot be read properly	The referenced images were moved or deleted (location path has changed)	(1) Make sure the referenced images are in the location designed in Nav_1.nav (2) Edit Nav_1.nav to reflect the updated location path for the missing images in a text editor program in Windows, i.e., Notepad
61	The ROI is not in the correlated position or is out of the field of view	(1) Registration in this correlated map is not updated (2) View and Record are not aligned (3) Pre-tilt angle is not correct	(1) Update the registration using the Shift to Marker function in the SerialEM Navigator menu (2) Align the View and Record by adjusting the offset in the Low Dose Control panel in SerialEM (3) Check the pre-tilt angles as in **49**
74	Automated stitching did not work	(1) The wrong scripts were used (2) Very thick areas where insufficient signal was preserved (3) Crystalline ice is present in >70% of overall view of the montage	(1) Check SerialEM version (4.1 or above) or (3.8 and 4.0). Run the scripts based on the SerialEM versions (2) Low-pass filter each tile view or use other preprocessing methods to enhance the features before stitching (3) Adjust the milling parameters aimed for thinner lamellae in AutoTEM (4) Change the blotting condition during the freezing or try adding cryoprotectants, i.e., 10% glycerol

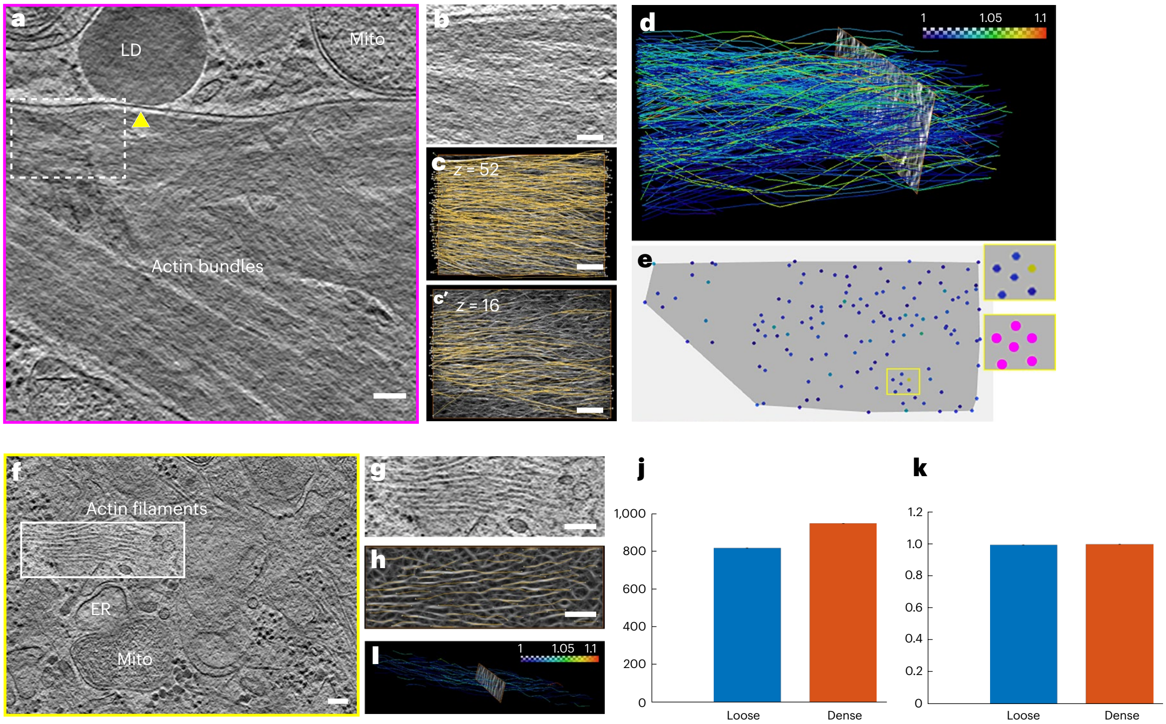

Fig. 14 | Representative segmentation analysis of distinct morphologies of actin-like filaments near the LD–mitochondrial site captured by MPACT. **a**–**e,** Actin-like filaments display densely packed (**a**–**e**, pink boxed region in Fig. 8k) and loosely packed (**f**–**i**, yellow boxed region in Fig. 8k) arrangements: a 20-nm-thick tomographic slice through a subcellular volume from the full 3 × 3 MPACT tomogram (Fig. 8k, pink box) (**a**); an enlarged view of the white boxed region in **a** (**b**); an overlay of actin tracing and segmentation at different *z* slices from the volume (*z* = 52 in **c** and *z* = 16 in **c'**); the corresponding segmentation of actin filaments, color coded from blue to red based on the tortuosity (**d**); and one cross-sectional segmentation view shows hexagon-like actin packing arrangements (delineated by pink circles in the zoomed-in view) (**e**). **f**, A 20-nm-thick tomographic slice through a subcellular volume from the full 3 × 3 MPACT tomogram (Fig. 8k, yellow boxed). **g**–**i**, An enlarged view of the white boxed region in **f** (**g**) and the corresponding actin segmentation overlay with the tracing (**h**) and color-coded display based on tortuosity (**i**) show the loosely packed morphology. **j**,**k**, Statistical characterization (mean ± s.d.) in length (**j**) and tortuosity (**k**) of the dense (red) and loose (blue) actin-like filaments around the lipid droplets–mitochondria sites to show the differences. Scale bars, 100 nm in **a**–**h**.

Anticipated results

Following this protocol, a researcher with prior experience in cryo-EM or cryo-ET can perform in-chamber fluorescence light microscopy-guided cryo-FIB milling to generate thin lamellae (200–250 nm thickness) in an automated and reliable manner (Figs. 1 and 8). Subsequently, montage cryo-ET via MPACT can be carried out to collect tilt series that preserve both large FOVs and high-resolution structural information (Figs. 8 and 14). The reconstructed stitched tomograms can be quantitatively analyzed using segmentation[75] and analysis tools[35]. For example, to capture the ultrastructural and morphological characterization of actin bundles surrounding targeted lipid droplets (LDs), where higher metabolic activities are often observed, we found densely packed actin in proximity to LDs. In contrast, loose actin filaments were spread out in the cytoplasm (Fig. 14). STA can be performed using either individual tile tilt series, as demonstrated previously[26], or stitched reconstructions. In practice, common issues include two targeted ROIs in two different *z* planes (Fig. 9a,b) and the presence of ice contamination above an ROI (Fig. 9d). In this example, two targeted ROIs were adjacent in the *xy* view. Still, the relative *z*-height difference was above the thickness of the final lamella, for example, ~200 nm, therefore making it impossible to preserve both ROIs (Fig. 9a). In such cases, we usually focus on one ROI via the single-pair ROI–marker correlation and look for other possible milling sites (Fig. 9e,f) while the material is being thinned. Instead of acquiring montage tilt series via MPACT, several individual cryo-ET tilt series can be collected when several target ROI are farther apart. In AutoTEM, the calculated milling box is typically positioned so that the ROI is centered within the lamella. We recommend adjusting the milling box to be at the same *z* height but position it slightly off center, this will still capture the ROI even when a target site is close to a cell edge (Fig. 9d). Other common issues are generally associated with insufficient sample vitrification, broken lamellae, and curtaining, which have all been described previously.

Reporting summary

Further information on research design is available in the Nature Portfolio Reporting Summary linked to this article.

Data availability

All relevant data are available from the corresponding author upon request. The iFLM image stacks and corresponding SEM and FIB images are associated with the on-the-fly 3D correlation procedure. While it is challenging to share, a demonstration could be performed to help the user upon reasonable request. A set of raw frames for a representative 3 × 3 MPACT montage tilt series is provided as a tutorial dataset and available to download at https://github.com/wright-cemrc-projects/cryoet-montage/tree/main/Tutorial/ for demonstration of MPACT preprocessing, stitching and individual tile tilt series generation. Subtomogram averages of respiratory syncytial virus fusion pair particles using MPACT individual tile tilt series have been deposited in the Electron Microscopy Data Bank under accession numbers EMD-40308 and EMD-40307.

Code availability

CorRelator and TomoGrapher are open-source software, and the source code can be downloaded via https://github.com/wright-cemrc-projects. The MPACT processing scripts can be downloaded via https://github.com/wright-cemrc-projects/cryoet-montage/tree/main/Bashscripts.

Received: 15 March 2025; Accepted: 25 September 2025;
Published online: 30 January 2026

References

1. Hong, Y., Song, Y., Zhang, Z. & Li, S. Cryo-electron tomography: the resolution revolution and a surge of in situ virological discoveries. *Annu. Rev. Biophys.* **52**, 339–360 (2023).
2. Turk, M. & Baumeister, W. The promise and the challenges of cryo-electron tomography. *FEBS Lett.* **594**, 3243–3261 (2020).
3. Al-Amoudi, A. et al. Cryo-electron microscopy of vitreous sections. *EMBO J.* **23**, 3583–3588 (2004).
4. Berger, C. et al. Cryo-electron tomography on focused ion beam lamellae transforms structural cell biology. *Nat. Methods* **20**, 499–511 (2023).
5. Rigort, A. et al. Micromachining tools and correlative approaches for cellular cryo-electron tomography. *J. Struct. Biol.* **172**, 169–179 (2010).
6. Hampton, C. M. et al. Correlated fluorescence microscopy and cryo-electron tomography of virus-infected or transfected mammalian cells. *Nat. Protoc.* **12**, 150–167 (2017).
7. Yang, J. E., Larson, M. R., Sibert, B. S., Shrum, S. & Wright, E. R. CorRelator: interactive software for real-time high precision cryo-correlative light and electron microscopy. *J. Struct. Biol.* **213**, 107709 (2021).
8. Smeets, M. et al. Integrated cryo-correlative microscopy for targeted structural investigation in situ. *Microsc. Today* **29**, 20–25 (2021).
9. Arnold, J. et al. Site-specific cryo-focused ion beam sample preparation guided by 3D correlative microscopy. *Biophys. J.* **110**, 860–869 (2016).
10. Hall, A. S., Lavery, L. L. & Doux, P. Effective multimodal multiscale analytical and imaging correlation. *IEEE Sens. Lett.* **3**, 1–4 (2019).
11. Moser, F. et al. Cryo-SOFI enabling low-dose super-resolution correlative light and electron cryo-microscopy. *Proc. Natl Acad. Sci. USA* **116**, 4804–4809 (2019).
12. Schorb, M. et al. New hardware and workflows for semi-automated correlative cryo-fluorescence and cryo-electron microscopy/tomography. *J. Struct. Biol.* **197**, 83–93 (2017).
13. Chang, Y.-W. et al. Correlated cryogenic photoactivated localization microscopy and cryo-electron tomography. *Nat. Methods* **11**, 737–739 (2014).
14. Fukuda, Y. et al. Coordinate transformation based cryo-correlative methods for electron tomography and focused ion beam milling. *Ultramicroscopy* **143**, 15–23 (2014).
15. Kelley, K. et al. Waffle Method: a general and flexible approach for improving throughput in FIB-milling. *Nat. Commun.* **13**, 1857 (2022).
16. Wolff, G. et al. Mind the gap: micro-expansion joints drastically decrease the bending of FIB-milled cryo-lamellae. *J. Struct. Biol.* **208**, 107389 (2019).
17. Booy, F. P. & Pawley, J. B. Cryo-crinkling: what happens to carbon films on copper grids at low temperature. *Ultramicroscopy* **48**, 273–280 (1993).
18. Li, W. et al. Integrated multimodality microscope for accurate and efficient target-guided cryo-lamellae preparation. *Nat. Methods* **20**, 268–275 (2023).
19. Li, S. et al. ELI trifocal microscope: a precise system to prepare target cryo-lamellae for in situ cryo-ET study. *Nat. Methods* **20**, 276–283 (2023).
20. Gorelick, S. et al. PIE-scope, integrated cryo-correlative light and FIB/SEM microscopy. *eLife* **8**, e45919 (2019).
21. Tacke, S. et al. A streamlined workflow for automated cryo focused ion beam milling. *J. Struct. Biol.* **213**, 107743 (2021).
22. Klumpe, S. et al. A modular platform for automated cryo-FIB workflows. *eLife* **10** (2021).
23. Zachs, T. et al. Fully automated, sequential focused ion beam milling for cryo-electron tomography. *eLife* **9** (2020).
24. Hylton, R. K. & Swulius, M. T. Challenges and triumphs in cryo-electron tomography. *iScience* **24**, 102959 (2021).
25. Schur, F. K. M. Toward high-resolution in situ structural biology with cryo-electron tomography and subtomogram averaging. *Curr. Opin. Struct. Biol.* **58**, 1–9 (2019).
26. Yang, J. E. et al. Correlative montage parallel array cryo-tomography for in situ structural cell biology. *Nat. Methods* **20**, 1537–1543 (2023).
27. Huang, Y.-W., Cambre, M. & Lee, H.-J. The toxicity of nanoparticles depends on multiple molecular and physicochemical mechanisms. *Int. J. Mol. Sci.* **18**, 2702 (2017).
28. Scher, N., Rechav, K., Paul-Gilloteaux, P. & Avinoam, O. In situ fiducial markers for 3D correlative cryo-fluorescence and FIB-SEM imaging. *iScience* **24**, 102714 (2021).
29. Yang, J. E., Mitchell, J. M., Bingman, C. A., Mosher, D. F. & Wright, E. R. In situ crystalline structure of the human eosinophil major basic protein-1. Preprint at *bioRxiv* https://doi.org/10.1101/2024.10.09.617336 (2024).
30. Kim, J. Y. et al. Handling difficult cryo-ET samples: a study with primary neurons from *Drosophila melanogaster*. *Microsc. Microanal.* **29**, 2127–2148 (2023).
31. Sibert, B. S., Kim, J. Y., Yang, J. E. & Wright, E. R. Micropatterning transmission electron microscopy grids to direct cell positioning within whole-cell cryo-electron tomography workflows. *J. Vis. Exp.* **175**, e62992 (2021).
32. Sibert, B. S. et al. Assembly of respiratory syncytial virus matrix protein lattice and its coordination with fusion glycoprotein trimers. *Nat. Commun.* **15**, 5923 (2024).
33. Mastronarde, D. N. Automated electron microscope tomography using robust prediction of specimen movements. *J. Struct. Biol.* **152**, 36–51 (2005).
34. Mastronarde, D. Tomographic reconstruction with the IMOD software package. *Microsc. Microanal.* **12**, 178–179 (2006).
35. Garza-Lopez, E. et al. Protocols for generating surfaces and measuring 3D organelle morphology using Amira. *Cells* **11**, 65 (2022).
36. Stalling, D., Westerhoff, M. & Hege, H.-C. in *The Visualization Handbook* (Academic Press, 2005).
37. Chen, M. et al. Convolutional neural networks for automated annotation of cellular cryo-electron tomograms. *Nat. Methods* **14**, 983–985 (2017).
38. Heebner, J. E. et al. Deep learning-based segmentation of cryo-electron tomograms. *J. Vis. Exp.* **189**, e64435 (2022).
39. Wan, W. & Briggs, J. A. Cryo-electron tomography and subtomogram averaging. *Methods Enzymol.* **579**, 329–367 (2016).
40. Castaño-Díez, D., Kudryashev, M., Arheit, M. & Stahlberg, H. Dynamo: a flexible, user-friendly development tool for subtomogram averaging of cryo-EM data in high-performance computing environments. *J. Struct. Biol.* **178**, 139–151 (2012).
41. Nicastro, D. et al. The molecular architecture of axonemes revealed by cryoelectron tomography. *Science* **313**, 944–948 (2006).
42. Bharat, T. A. M. & Scheres, S. H. W. Resolving macromolecular structures from electron cryo-tomography data using subtomogram averaging in RELION. *Nat. Protoc.* **11**, 2054–2065 (2016).
43. Wagner, F. R. et al. Preparing samples from whole cells using focused-ion-beam milling for cryo-electron tomography. *Nat. Protoc.* **15**, 2041–2070 (2020).
44. Boltje, D. B. et al. A cryogenic, coincident fluorescence, electron, and ion beam microscope. *eLife* **11**, e82891 (2022).
45. Schiøtz, O. H. et al. Serial Lift-Out: sampling the molecular anatomy of whole organisms. *Nat. Methods* **21**, 1684–1692 (2023).
46. Paul-Gilloteaux, P. et al. eC-CLEM: flexible multidimensional registration software for correlative microscopies. *Nat. Methods* **14**, 102–103 (2017).
47. Schorb, M. & Briggs, J. A. Correlated cryo-fluorescence and cryo-electron microscopy with high spatial precision and improved sensitivity. *Ultramicroscopy* **143**, 24–32 (2014).
48. Kukulski, W. et al. Correlated fluorescence and 3D electron microscopy with high sensitivity and spatial precision. *J. Cell Biol.* **192**, 111–119 (2011).
49. Peck, A. et al. Montage electron tomography of vitrified specimens. *J. Struct. Biol.* **214**, 107860 (2022).
50. Elferich, J., Schiroli, G., Scadden, D. T. & Grigorieff, N. Defocus Corrected Large Area Cryo-EM (DeCo-LACE) for label-free detection of molecules across entire cell sections. *eLife* **11**, e80980 (2022).
51. Chua, E. Y. D. et al. Square beams for optimal tiling in transmission electron microscopy. *Nat. Methods* **21**, 562–565 (2024).
52. Brown, H. G., Smith, D., Wardle, B. C. & Hanssen, E. Square condenser apertures for square cameras in low-dose transmission electron microscopy. *Nat. Methods* **21**, 566–568 (2024).
53. Eisenstein, F. et al. Parallel cryo electron tomography on in situ lamellae. *Nat. Methods* **20**, 131–138 (2023).
54. Bouvette, J. et al. Beam image-shift accelerated data acquisition for near-atomic resolution single-particle cryo-electron tomography. *Nat. Commun.* **12**, 1957 (2021).
55. Eisenstein, F., Danev, R. & Pilhofer, M. Improved applicability and robustness of fast cryo-electron tomography data acquisition. *J. Struct. Biol.* **208**, 107–114 (2019).
56. Chreifi, G., Chen, S., Metskas, L. A., Kaplan, M. & Jensen, G. J. Rapid tilt-series acquisition for electron cryotomography. *J. Struct. Biol.* **205**, 163–169 (2019).
57. Sexton, D. L., Burgold, S., Schertel, A. & Tocheva, E. I. Super-resolution confocal cryo-CLEM with cryo-FIB milling for in situ imaging of *Deinococcus radiodurans*. *Curr. Res. Struct. Biol.* **4**, 1–9 (2022).
58. Weber, N., Hinks, B., Jensen, J., Lidahl, T. & Mendonça, L. Sample preparation for in situ cryotomography of mammalian cells. *J. Vis. Exp.* **202**, e65697 (2023).
59. Thompson, R. F., Walker, M., Siebert, C. A., Muench, S. P. & Ranson, N. A. An introduction to sample preparation and imaging by cryo-electron microscopy for structural biology. *Methods* **100**, 3–15 (2016).
60. de Beer, M. et al. Precise targeting for 3D cryo-correlative light and electron microscopy volume imaging of tissues using a FinderTOP. *Commun. Biol.* **6**, 510 (2023).
61. Toro-Nahuelpan, M. et al. Tailoring cryo-electron microscopy grids by photo-micropatterning for in-cell structural studies. *Nat. Methods* **17**, 50–54 (2020).
62. Bäuerlein, F. J. B. et al. Cryo-electron tomography of large biological specimens vitrified by plunge freezing. Preprint at *bioRxiv* https://doi.org/10.1101/2021.04.14.437159 (2023).
63. Hands-Portman, I. & Bakker, S. E. Customising the plunge-freezing workflow for challenging conditions. *Faraday Discuss.* **240**, 44–54 (2022).
64. Tuijtel, M. W., Koster, A. J., Jakobs, S., Faas, F. G. A. & Sharp, T. H. Correlative cryo super-resolution light and electron microscopy on mammalian cells using fluorescent proteins. *Sci. Rep.* **9**, 1369 (2019).
65. Metskas, L. A. & Briggs, J. A. G. Fluorescence-based detection of membrane fusion state on a cryo-EM grid using correlated cryo-fluorescence and cryo-electron microscopy. *Microsc. Microanal.* **25**, 942–949 (2019).
66. Karuppasamy, M., Karimi Nejadasl, F., Vulovic, M., Koster, A. J. & Ravelli, R. B. Radiation damage in single-particle cryo-electron microscopy: effects of dose and dose rate. *J. Synchrotron Radiat.* **18**, 398–412 (2011).
67. Basanta, B., Hirschi, M. M., Grotjahn, D. A. & Lander, G. C. A case for glycerol as an acceptable additive for single-particle cryoEM samples. *Acta Crystallogr. D.* **78**, 124–135 (2022).

68. Melo, R. C. N. & Weller, P. F. Contemporary understanding of the secretory granules in human eosinophils. *J. Leukoc. Biol.* **104**, 85–93 (2018).
69. Grant, T. & Grigorieff, N. Measuring the optimal exposure for single particle cryo-EM using a 2.6 Å reconstruction of rotavirus VP6. *eLife* **4**, e06980 (2015).
70. Zheng, S. Q. et al. MotionCor2: anisotropic correction of beam-induced motion for improved cryo-electron microscopy. *Nat. Methods* **14**, 331–332 (2017).
71. Chen, M. et al. A complete data processing workflow for cryo-ET and subtomogram averaging. *Nat. Methods* **16**, 1161–1168 (2019).
72. Tegunov, D., Xue, L., Dienemann, C., Cramer, P. & Mahamid, J. Multi-particle cryo-EM refinement with M visualizes ribosome-antibiotic complex at 3.5 Å in cells. *Nat. Methods* **18**, 186–193 (2021).
73. Dimchev, G., Amiri, B., Fäßler, F., Falcke, M. & Schur, F. K. Computational toolbox for ultrastructural quantitative analysis of filament networks in cryo-ET data. *J. Struct. Biol.* **213**, 107808 (2021).
74. Lam, V. & Villa, E. Practical approaches for cryo-FIB milling and applications for cellular cryo-electron tomography. *Methods Mol. Biol.* **2215**, 49–82 (2021).
75. Rigort, A. et al. Automated segmentation of electron tomograms for a quantitative description of actin filament networks. *J. Struct. Biol.* **177**, 135–144 (2012).
76. Morin, A. et al. Collaboration gets the most out of software. *eLife* **2**, e01456 (2013).
77. Schaffer, M. et al. Optimized cryo-focused ion beam sample preparation aimed at in situ structural studies of membrane proteins. *J. Struct. Biol.* **197**, 73–82 (2017).
78. Langford, R. M. Focused ion beam nanofabrication: a comparison with conventional processing techniques. *J. Nanosci. Nanotechnol.* **6**, 661–668 (2006).

Acknowledgements

We are grateful for the TEM and SEM instrumentation support of M. Woods and T. Coomes from Thermo Fisher Scientific. We are thankful for the computational resources supplied through the SBGrid[76]. This work was supported in part by the University of Wisconsin, Madison, the Department of Biochemistry at the University of Wisconsin, Madison, the Morgridge Institute for Research, and public health service grant nos. R01 GM114561, R01 GM132068, RF1 NS110436 and U24 GM139168 to E.R.W., P01 HL088594 to N. Jarjour, and R01 AI125390 to D.F.M. and J. Coon from the National Institutes of Health. J.M.M. was supported by the grant T32 HL07899 from the National Heart, Lung, and Blood Institute, National Institutes of Health. This work was supported in part by the US Department of Energy, Office of Science, Office of Biological and Environmental Research under award number DE-SC0018409. We are grateful for the use of facilities and instrumentation at the Cryo-EM Research Center and the Midwest Center for Cryo-ET in the Department of Biochemistry at the University of Wisconsin, Madison.

Author contributions

E.R.W., J.M., J.E.Y., V.V., T.F. and A.R. conceived the study. J.E.Y. and E.R.W. designed the study. J.E.Y., V.V., B.S.S., J.M.M., T.F., A.S.H., A.R., M.R.L., D.F.M., J.M. and E.R.W. prepared the samples, performed the experiments and processed the data. J.E.Y. and E.R.W. wrote the manuscript with contributions from all authors. All authors read and approved the manuscript.

Competing interests

V.V., T.F., A.H., A.R. and J.M. are employees of Thermo Fisher Scientific. Other authors have no competing interests or other interests that might be perceived to influence the interpretation of the article.

Additional information

Supplementary information The online version contains supplementary material available at https://doi.org/10.1038/s41596-025-01284-z.

Correspondence and requests for materials should be addressed to Elizabeth R. Wright.

Peer review information *Nature Protocols* thanks Johannes Groen, Michael Martynowycz and Anna Steyer for their contribution to the peer review of this work.

nature research

Corresponding author(s): NP-P230749B_Wright

Last updated by author(s): Aug 29, 2025

Reporting Summary

Nature Research wishes to improve the reproducibility of the work that we publish. This form provides structure for consistency and transparency in reporting. For further information on Nature Research policies, see our Editorial Policies and the Editorial Policy Checklist.

Statistics

For all statistical analyses, confirm that the following items are present in the figure legend, table legend, main text, or Methods section.

n/a	Confirmed	
☐	☒	The exact sample size (*n*) for each experimental group/condition, given as a discrete number and unit of measurement
☐	☒	A statement on whether measurements were taken from distinct samples or whether the same sample was measured repeatedly
☐	☒	The statistical test(s) used AND whether they are one- or two-sided *Only common tests should be described solely by name; describe more complex techniques in the Methods section.*
☒	☐	A description of all covariates tested
☐	☒	A description of any assumptions or corrections, such as tests of normality and adjustment for multiple comparisons
☐	☒	A full description of the statistical parameters including central tendency (e.g. means) or other basic estimates (e.g. regression coefficient) AND variation (e.g. standard deviation) or associated estimates of uncertainty (e.g. confidence intervals)
☒	☐	For null hypothesis testing, the test statistic (e.g. *F*, *t*, *r*) with confidence intervals, effect sizes, degrees of freedom and *P* value noted *Give P values as exact values whenever suitable.*
☒	☐	For Bayesian analysis, information on the choice of priors and Markov chain Monte Carlo settings
☒	☐	For hierarchical and complex designs, identification of the appropriate level for tests and full reporting of outcomes
☒	☐	Estimates of effect sizes (e.g. Cohen's *d*, Pearson's *r*), indicating how they were calculated

Our web collection on statistics for biologists contains articles on many of the points above.

Software and code

Policy information about availability of computer code

Data collection	The integrated FLM image stacks were collected and tested using iFLM software (ThermoFisher Scientific) v 1. 3. 0 and v. 1.4.0. and 1.4.1. All versions work well with the workflow presented here. Maps software v. 3.20, v. 3.25, v. 3.29, v. 3.30, v. 3.32 (ThermoFisher Scientific) and AutoTEM v. 2.4.0, v. 2.4.2 (ThermoFisher Scientific) were used. All versions work well with the workflow. xT software and server v 32.1. 1 (ThermoFisher Scientific) was used. SerialEM v. 3.8, v. 4.0, v. 4.1 were used and all worked well. MPACT acquisition (https://github.com/wright-cemrc-projects/cryoet-montage/tree/main/SerialEM) TomoGrapher installation can be found here (https://github.com/wright-cemrc-projects/cryoet-montage/tree/main/TomoGrapher) CorRelator v 1.30, v 1.40 can be found here (https://github.com/wright-cemrc-projects/corr) Optional: Leica LASX CORAL(v. 4.6.2.28352) was used for external cryo-CLEM integration with the downstream Maps-AutoTEM platforms.
Data analysis	MotionCor2, IMOD, Dynamo , Isonet can be managed via SBGrid Consortium (https://sbgrid.org/) MotionCor2 (UCSF, USA), IMOD v. 4.11, MATLAB (R2020, R2022, R2024) were used for downstream MPACT data preprocessing MPACT preprocessing scripts can be found here for SerialEM v. 4.1 and above (strongly recommended, https://github.com/wright-cemrc-projects/cryoet-montage/tree/main/Bashscripts) and for SerialEM v. 3.8 and 4.0 can be found here (https://github.com/wright-cemrc-projects/cryoet-montage/tree/main/Python). Isonet v. 0.2 (https://github.com/IsoNet-cryoET/IsoNet) was used to denoise the tomograms. Fiji (PSF based processing algorithm such as Richardson-Lucy in DeconvolutionLab2) fluorescent image processing was used. Amira 3D 2023.2 (ThermoFisher Scientific) Computational toolbox for ultrastructural quantitative analysis of filament networks in cryo-ET (https://schurlab.ist.ac.at/downloads/)

Dynamo v. 1.1.511 was used for subtomogram averaging
Prism v 10.5.0 (673) (GraphPad, USA) was used to plot the correlation precision deviation.
Adobe Illustrator 2023 and above was used to generate the figures

For manuscripts utilizing custom algorithms or software that are central to the research but not yet described in published literature, software must be made available to editors and reviewers. We strongly encourage code deposition in a community repository (e.g. GitHub). See the Nature Research guidelines for submitting code & software for further information.

Data

Policy information about availability of data

All manuscripts must include a data availability statement. This statement should provide the following information, where applicable:

- Accession codes, unique identifiers, or web links for publicly available datasets
- A list of figures that have associated raw data
- A description of any restrictions on data availability

The subtomogram averages for MPACT have been deposited under EMD-40308, EMD-40307 as described from the previous publication (Yang et al. Nat Methods, 2023, PMID:37723245)

Field-specific reporting

Please select the one below that is the best fit for your research. If you are not sure, read the appropriate sections before making your selection.

☒ Life sciences ☐ Behavioural & social sciences ☐ Ecological, evolutionary & environmental sciences

For a reference copy of the document with all sections, see nature.com/documents/nr-reporting-summary-flat.pdf

Life sciences study design

All studies must disclose on these points even when the disclosure is negative.

Sample size	The samples used for 3D single-pair ROI-Marker targeted milling were mammalian cells including HeLa cells (XY: (40~80)^2 µm^2 and Z: 12~18 µm), A549 cells (XY: (40~80) µm^2 and Z: 15~20 µm), human mature eosinophils (XY: (8-10)^2 um^2 and Z: 5~10 µm), Yeast cells (XY: 12~16 µm and Z: 1.5~2 µm)
Data exclusions	No data was exluded
Replication	The overall 3D targeting precision retainment success rate for biological samples has been performed on 117 targets from 12 independently. performed experiments. 5 x 2 independently performed fiducial targeting were performed with (n > 5) for room temperature and cryogenic condition baseline 3D targeting, respectively.
Randomization	The grids used for 3D targeted milling for each sample type were randomly chosen from 4 to 8 grids that were prepared at least 3 times sample preparation/freezing sessions
Blinding	The grids chosen and target chosen for each sample type were blind and the calculation for target precision is also blind.

Reporting for specific materials, systems and methods

We require information from authors about some types of materials, experimental systems and methods used in many studies. Here, indicate whether each material, system or method listed is relevant to your study. If you are not sure if a list item applies to your research, read the appropriate section before selecting a response.

Materials & experimental systems

n/a	Involved in the study
☒	☐ Antibodies
☐	☒ Eukaryotic cell lines
☒	☐ Palaeontology and archaeology
☐	☒ Animals and other organisms
☒	☐ Human research participants
☒	☐ Clinical data
☒	☐ Dual use research of concern

Methods

n/a	Involved in the study
☒	☐ ChIP-seq
☒	☐ Flow cytometry
☒	☐ MRI-based neuroimaging

Eukaryotic cell lines

Policy information about cell lines

Cell line source(s)	ATCC
Authentication	Authenticated through ATCC upon purchasing
Mycoplasma contamination	No contamination
Commonly misidentified lines (See ICLAC register)	N/A

Animals and other organisms

Policy information about studies involving animals; ARRIVE guidelines recommended for reporting animal research

Laboratory animals	No animals were used. Yeast were modified cultured lab strain (BSL-1) from the users in the National Midwest Center for Cryo-ET
Wild animals	No wild animals were used
Field-collected samples	Human eosinophil cells were obtained from donors for studies that were approved by the University of Wisconsin-Madison Health Sciences Institutional Review Board (protocol no. 2013-1570). Informed written consent was obtained before participation.
Ethics oversight	University of Wisconsin-Madison Health Sciences Institutional Review Board approved the use of human eosinophils in this study.

Note that full information on the approval of the study protocol must also be provided in the manuscript.